Computational Mechanics
https://doi.org/10.1007/s00466-025-02692-4

ORIGINAL PAPER

A self-contact electromechanical framework for intestinal motility

René Thierry Djoumessi[1] · **Pietro Lenarda**[1] · **Alessio Gizzi**[2] · **Marco Paggi**[1]

Received: 3 June 2025 / Accepted: 31 August 2025

Abstract
This study introduces a comprehensive multiphysics and multiscale modeling framework for simulating intestinal motility, explicitly incorporating the effects of contact mechanics. The proposed approach couples finite elasticity electromechanics, which captures the microstructural architecture and mechanical behavior of the intestinal wall, with tissue-level electrophysiology, enabling the representation of slow wave propagation and active contractile dynamics. To model mechanical interactions accurately, the framework integrates a self-contact detection algorithm that combines a nearest-neighbor search strategy with the penalty method, ensuring robust enforcement of non-interpenetration constraints. In addition, the model accommodates inhomogeneous boundary conditions that simulate the mechanical influence of adjacent organs on the intestinal tissue. The active strain governing equations are solved via a staggered finite element scheme, implemented within the open-source `FEniCS` environment. The model is applied to clinically relevant scenarios, including moderate and severe strangulation hernia as well as intestinal adhesion syndrome. Simulation results reveal a marked reduction in peristaltic activity in pre-strangulation regions, accompanied by elevated intraluminal pressure in the strangulated segment. In cases of self-adhesion, the model predicts a complete suppression of motility within the adherent zone. Overall, the computational analyses successfully reproduce the spatiotemporal dynamics of electromechanical wave propagation under conditions of distributed contact boundaries, representative of pre- and post-surgical states. The proposed framework demonstrates significant potential for advancing our understanding of self-contact in active soft tissues, and provides a valuable tool for predicting and analyzing motility disorders in the gastrointestinal tract.

Keywords Finite element · Contact search method · Active strain · Electromechanics · Intestinal motility · Manometry · Strangulated hernia

1 Introduction

1.1 Biomechanical bases

The intestine, a vital component of the digestive tract, plays a crucial role in processing food and absorbing nutrients. It is divided into two main sections: the small intestine and the large intestine. The small intestine is primarily responsible for absorbing the majority of nutrients and breaking down food into its essential components, including proteins, carbohydrates, and fats. Once most nutrients have been absorbed, the remaining undigested food residues, or chyme, pass into the large intestine. The large intestine primary function is to absorb water, electrolytes, and vitamins produced by gut bacteria while also compacting waste into the stool for elimination [1–3]. However, our understanding of the mechanisms behind the different types of movement, such as peristalsis and segmentation, remains incomplete,

✉ René Thierry Djoumessi
rene.djoumessi@imtlucca.it

✉ Pietro Lenarda
pietro.lenarda@imtlucca.it

Alessio Gizzi
a.gizzi@unicampus.it

Marco Paggi
marco.paggi@imtlucca.it

[1] IMT School for Advanced Studies Lucca, Piazza San Francesco 19, 55100 Lucca, Italy

[2] Department of Engineering, Università Campus Bio-Medico di Roma, Via A. del Portillo 21, 00128 Rome, Italy

Published online: 24 September 2025

making their modeling and prediction extremely complex. Over the last two decades, multiphysics and multiscale models have been proposed to understand better intestine electrophysiology [4–6], passive mechanics [7, 8], and active electromechanics [9–11]; however, gastrointestinal biomechanics lags 20 years back towards cardiovascular research. Current effort aims at filling the gap with advanced experimental settings [12–14].

Unlike organs such as the heart and lungs, which are protected by the rib cage, the intestine lacks a rigid structural enclosure and is thus relatively free to move within the abdominal cavity. Nevertheless, its position is regulated by various anatomical structures, primarily the mesentery and the abdominal wall, which apply mechanical constraints and exert pressure to prevent the intestine from displacing or "falling" within the cavity [15, 16]. To date, electromechanical models of intestinal motility have not incorporated these physical interactions–unlike those developed for cardiac modeling [17]. Furthermore, post-surgical complications are common, affecting over 90% of patients following abdominal surgery [18]. These complications often involve fibrous scar tissue or adhesions that increase local stiffness and impair intestine motility [19–21]. One of the most severe outcomes is hernia, in which a portion of the intestine protrudes into another abdominal compartment, potentially leading to strangulation [22–24].

External forces–such as pressure from surrounding organs–or pathological conditions can significantly influence intestinal mechanics, often resulting in undesirable self-contact or adhesions between adjacent bowel segments [25]. Although numerous algorithms exist in the literature for modeling contact mechanics under both small and large deformation regimes, including self-contact scenarios [26–28], none have yet been applied to characterize intestinal motility driven by electromechanical contractions. Therefore, the present work aims at filling this important methodological gap in the literature.

1.2 Contact mechanics

Among the various methods used to enforce the non-penetration constraint during contact, the penalty method is one of the most widely adopted due to its computational simplicity and ease of implementation [29–31]. This approach introduces an artificial restoring force proportional to the penetration depth, thereby promoting compliance with the non-interpenetration condition. Its straightforward formulation makes it especially well-suited for integration into finite element frameworks, while maintaining robustness across a broad range of contact scenarios [30]. However, the method accuracy and numerical stability are highly dependent on the choice of the penalty parameter: a value that is too low may permit significant interpenetration, while an excessively high value can result in increased artificial contact stiffness and potential numerical instability.

Search algorithms commonly used in contact mechanics are often computationally intensive. The standard approach for computing relative distances between two discretized contact surfaces has a typical computational complexity of order $O(N^2)$, as it requires evaluating the distance from each point on one surface to all points on the opposing surface. To reduce this cost, several acceleration strategies have been developed, tailored to the characteristics of the contact problem and the representation of the surfaces [32–35]. Among these, one approach models the gap function as the solution to a screened Poisson equation [28], while another interprets the gap as a phase field derived from an Eulerian diffused interface formulation [36]. Additionally, a third medium method improves upon the formulation proposed by Wriggers [37] by introducing a regularization scheme that stabilizes the medium. Under compression, the third medium naturally develops a reaction force opposing the compression; the regularization prevents numerical blow-up, thereby eliminating the need for explicit gap computation [38, 39].

In the present work, we propose an alternative strategy based on the k-d (k-dimensional) tree Nearest-Neighbor algorithm, which offers a more efficient and scalable means of detecting contact interactions [40, 41].

In computer science, a k-d tree is a space-partitioning data structure used to organize points in a k-dimensional space with respect to k orthogonal axes. It is well-suited for managing data in spaces of any dimensionality and is particularly effective for applications that involve multidimensional search keys, such as range searches and nearest-neighbor queries, as well as for generating point clouds used in clustering problems. In computer vision, k-d trees are widely applied to match keypoints across images by efficiently identifying the nearest neighbors of feature descriptors such as SIFT or SURF, enabling tasks like image stitching and 3D reconstruction [42]. In machine learning, k-d trees support algorithms such as k-nearest neighbors (k-NN) for classification and regression, by structuring high-dimensional feature spaces to enable fast and scalable neighbor searches [40, 43].

In the context of computing minimal distances between contact surfaces, k-d tree optimization reduces the distance evaluation cost to only the nearest points on the opposing surface, significantly lowering the computational complexity to $O(N \log(N))$ while maintaining sufficient accuracy for modeling contact interactions.

1.3 Large deformations and self-contact

In large deformation settings, the incompressibility of biological tissues is typically handled via a fully incompressible formulation or a nearly incompressible formulation. To avoid volumetric locking–a common issue in standard displacement-based finite elements–alternative formulations are employed. In the fully incompressible case, a two-field formulation (displacement–pressure) is standard, where pressure acts as a Lagrange multiplier. For the nearly incompressible case, both two-field and three-field (displacement–pressure–volume change) formulations are used, depending on the approximation and stabilization method. These strategies decouple volumetric and deviatoric deformations, mitigating locking. A recent study [44] on intestinal biomechanics showed that the two-field formulation in the fully incompressible case offers the best trade-off between accuracy and efficiency. Based on these findings, this work adopts the two-field incompressible approach to accurately model soft tissue mechanics while avoiding volumetric locking.

Although self-contact is inherently a complex problem–often addressed in commercial software via heuristic-based algorithms–its difficulty increases substantially under large deformation conditions. While many existing models claim to accommodate finite strain regimes, they frequently rely on simplified constitutive laws such as Neo-Hookean or Saint-Venant-Kirchhoff formulations [45, 46]. These models, though capable of capturing geometric nonlinearity, behave almost linearly at the material level, thereby limiting their ability to predict complex mechanical responses. The challenge becomes even more pronounced when the strain energy function includes anisotropic contributions. Specifically, the presence of fiber-reinforced microstructures introduces direction-dependent stiffening and nonlinear, strain-sensitive behavior [47]. For example, sudden shortening or buckling of fibers along particular orientations can lead to highly localized deformations, bringing adjacent mesh nodes into near face-to-face proximity. This can cause face inversion, mesh entanglement, or other numerical instabilities, thereby complicating the accurate simulation of contact and large deformation phenomena [30, 48].

To address this gap, the present study introduces a generalized active strain electromechanical framework for modeling intestinal segments, explicitly accounting for self-contact under large deformations. We propose a geometrically robust strategy that overcomes common challenges in self-contact detection for highly deformed configurations. Instead of allowing nodes on the same surface to detect gaps among themselves-a method prone to ambiguity and numerical instability-we implement a systematic geometric criterion that prevents self-interaction between neighboring nodes on the same side of the structure. This approach enhances numerical stability and mitigates sensitivity to local folding and fiber-induced non-uniformities in the deformation field. Furthermore, the proposed model enables in silico analysis of specific pathological conditions, providing a computational platform to investigate the effects of diseases or surgical interventions on overall intestinal motility. This framework lays the groundwork for a deeper understanding of gastrointestinal dysfunctions and supports the development of clinically relevant predictive tools.

The manuscript is structured as follows: Sect. 2 revisits the generalized electromechanical framework for intestinal motility, extending the authors previous work [11] by incorporating a self-contact formulation. Section 3 derives the strong form of the governing equations and outlines the corresponding finite element discretization. In Sect. 4, a series of numerical experiments are presented to evaluate the model capabilities, including simulations that explore the influence of surrounding organs on gastrointestinal (GI) motility under two clinically relevant scenarios: herniation and adhesion syndrome. Finally, Sect. 5 summarizes the main findings, discusses current limitations, and outlines future research directions.

2 Intestine electromechanics and self-contact

In this section, we briefly recall the governing equations for active strain finite deformations coupled with GI electrophysiology.

We represent a scalar, a vector, and a second-order tensor with the lowercase letters (a), lowercase bold letters ($\boldsymbol{a}$), and capital bold letters ($\boldsymbol{A}$), respectively, and ($\boldsymbol{A}^T$) stands for the transpose of a tensor. According to the tensor notation, we indicate the scalar product with $(\cdot)$, the double contraction with $(:)$, and the dyadic product with $(\otimes)$. Moreover, ∇, $\nabla\cdot$ and ∇^2 represent the gradient, divergence, and Laplace operator, respectively.

2.1 Finite kinematics

Kinematics of deformable GI tissue is embedded in the classical description of continuum mechanics under the assumption of finite elasticity [49].

Let $\boldsymbol{X}$, $\boldsymbol{x}$ be the material position vector in the undeformed and deformed configuration Ω_0, $\Omega_t \subset R^d$, $d = 2, 3$ respectively, the deformation map ϕ is such that $\boldsymbol{x} = \phi(\boldsymbol{X})$, and the displacement field $\boldsymbol{u}$ is defined as $\boldsymbol{u} = \boldsymbol{x} - \boldsymbol{X}$. The deformation gradient tensor and its associated Jacobian are denoted as $\boldsymbol{F} = \partial\boldsymbol{x}/\partial\boldsymbol{X}$ and $J = \det \boldsymbol{F} > 0$, the right Cauchy-Green deformation tensor with $\boldsymbol{C} = \boldsymbol{F}^T\boldsymbol{F}$, the first

isotropic invariant of deformation with $I_1(\boldsymbol{C}) = \mathrm{tr}\,(\boldsymbol{C})$, where $\mathrm{tr}\,(\cdot)$ is the trace operator, and the fourth anisotropic pseudo-invariant is $I_4(\boldsymbol{C}) = \boldsymbol{C} : \boldsymbol{G}$, where $\boldsymbol{G}$ denotes the fiber structure tensor.

The contraction of the intestine combines active and passive behaviours, coupling electrophysiological cellular dynamics with a hyperelastic response of the material in a nonlinear manner. The active strain approach [9, 50, 51] remains an effective way for this type of coupling. In particular, the deformation gradient tensor is multiplicatively decomposed into an elastic part, $\boldsymbol{F}_e$, and an inelastic part, $\boldsymbol{F}_a$, as $\boldsymbol{F} = \boldsymbol{F}_e\boldsymbol{F}_a$ [11].

2.2 Electrophysiology

Intestinal motility is driven by slow wave activity generated by the interplay between interstitial cells of Cajal (ICCs) and smooth muscle cells (SMCs) [52–54]. Several models have been proposed to reproduce the key features of gastrointestinal electrical activity [10, 55, 56]. Electrical signals generated by ICCs propagate through gap junctions [57], triggering calcium influx in SMCs via voltage-gated channels [53], ultimately leading to smooth muscle contraction and wall deformation. We consider a simplified phenomenological model of intestine electrophysiology [4]. The SMCs and ICCs layers are denoted by the indices *s* and *i*, respectively. The resulting coupled reaction-diffusion system describing the interaction between transmembrane potential variables, u_s, u_i, and local slow current variables, v_s, v_i is given by two coupled FitzHugh-Nagumo-like formulations:

$$\frac{\partial u_s}{\partial t} = f(u_s) + D_s\nabla^2 u_s - v_s + F_s(u_s, u_i), \tag{1}$$

$$\frac{\partial v_s}{\partial t} = \epsilon_s[\lambda_s(u_s - \beta_s) - v_s], \tag{2}$$

$$\frac{\partial u_i}{\partial t} = g(u_i) + D_i\nabla^2 u_i - v_i + F_i(u_s, u_i) + I^i_{stim}, \tag{3}$$

$$\frac{\partial v_i}{\partial t} = \epsilon_i(z)[\lambda_i(u_i - \beta_i) - v_i], \tag{4}$$

with nonlinear bistable reactions and coupling functions:

$$\begin{aligned} f(u_s) &= k_s u_s(u_s - a_s)(1 - u_s)\,, \\ F_s(u_s, u_i) &= \alpha_s D_{si}(u_s - u_i)\,, \end{aligned} \tag{5}$$

$$\begin{aligned} g(u_i) &= k_i u_i(u_i - a_i)(1 - u_i)\,, \\ F_i(u_s, u_i) &= \alpha_i D_{is}(u_s - u_i)\,. \end{aligned} \tag{6}$$

Here, I^i_{stim} is the external current applied to the ICC layer; D_s, D_i represent spatiotemporal diffusivities; λ_s, λ_i are the coupling factors between the membrane potential and recovery variable; D_{si}, D_{is} couple the two cell species; $k_i, k_s, a_s, a_i, \alpha_s, \alpha_i$ are phenomenological model parameters and their values are provided in Table 2. The parameter $\epsilon(z)$ represents a space-dependent excitability function, decreasing with distance from the pylorus (details in [4, 11, 58]) and critical to activate the computational domain in the aboral direction.

2.3 Constitutive mechanical model

Following usual formulations for soft tissue biomechanics, we consider the intestinal wall as an anisotropic incompressible material. The tissue is reinforced by four families of fibers with specific preferential directions (see Fig. 1 for details). Accordingly, the strain energy density, Ψ, comprises isotropic, Ψ^{iso}, and anisotropic, Ψ^{aniso}, contributions. For the sake of simplicity, the isotropic part is considered of neo-Hookean type, while the anisotropic part is modeled as a variant Ogden-Holzapfel structure-based energy density accounting both for passive and active components used by

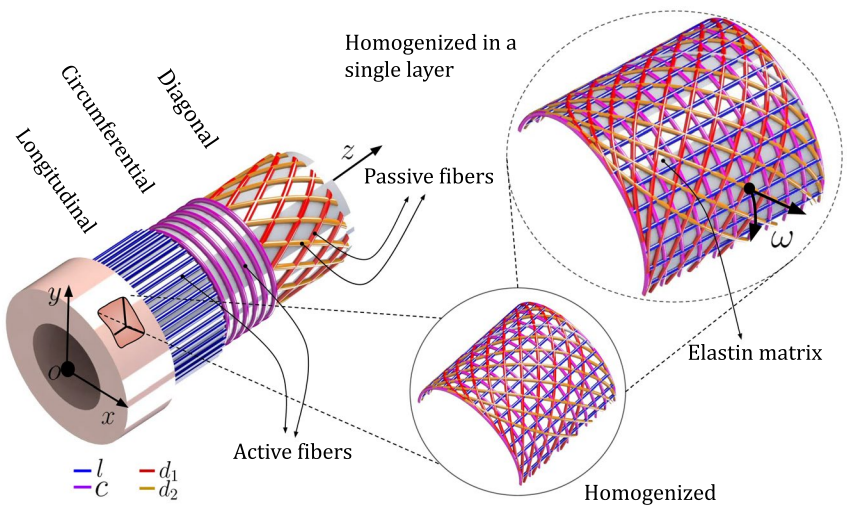

Fig. 1 Schematic segment of the intestine. The zoomed cross-section represents the homogenized fiber microstructure, which is composed of four families of fibers embedded in an isotropic elastin matrix. The directions of the fibers are uniquely defined with respect to the circumferential direction by the angle ω; *l* represents the external longitudinal muscular layer, *c* the internal circumferential muscular fiber, d_1 and d_2 are the submucosal diagonally collagen fibers

[8, 59]. The passive part is associated with the mechanical response of directional collagen fibers in the submucosal layer (d_1, d_2), while the active contribution is due to the presence of SMC fibers in the longitudinal (l) and circumferential (c) directions and is the only part contributing to the active deformation gradient $\boldsymbol{F}_a$ [11]:

$$\Psi = \Psi^{\text{iso}} + \Psi^{\text{aniso}} = \mu(I_1 - 3) + \sum_{i\in\{l,c,d_1,d_2\}} \frac{k_1^i}{4k_2^i}[e^{k_2^i\langle I_4^i-1\rangle^2} - 1] - p(J-1). \tag{7}$$

Here, the notation $\langle\mathcal{J}\rangle = (|\,\mathcal{J}\,| + \mathcal{J})/2$ stands for the Mackauley operator computing the positive part of $I_4^i - 1$, refers to the tension-compression switch approximation [60] and the anisotropic fourth invariant $I_4^j = \boldsymbol{C} : \boldsymbol{G}$, with $\boldsymbol{G} = (\boldsymbol{n}_j \otimes \boldsymbol{n}_j)$, is distinguished for each fiber family $j \in \{l, c, d_1, d_2\}$. The material parameters k_1^j (stiffness-like), k_2^j (nondimensional) are associated with the directional behavior, μ is the passive isotropic stiffness and p stands for the solid hydrostatic pressure in the fully incompressibility approach. The orientation of the fibers is generated using a Laplace-Dirichlet rule-based algorithm detailed in our previous work [11].

2.4 Modeling of the self-contact

2.4.1 Penalty approach to contact

Nonconforming contact problems require the identification of the contact area, which is not known a-priori, and the situation is even more challenging under a large deformation setting [46]. To address these problems, several advanced methods have been developed such as the Mortar method [61–63]. The most commonly used are still based on the master–slave configuration [32, 64, 65]. Major difficulties arise in the cases of self-contact and multi-body contacts under large displacements, where it is impossible or impractical to designate a master and a slave surface a priori, due to the continuous evolution of the contact scenario. To reduce these difficulties, some unbiased formulations for contact have been proposed in [66, 67]. In this work, an unbiased (no master and slave concept) version based on a penalty approach in large deformation has been pursued . Given that the GI system is mostly surrounded by fluids and is naturally lubricated to some extent, which reduces friction, we focused on a frictionless contact.

Our strategy (see Fig. 2) aims to prevent any interpenetration between the two surfaces Γ_c in contact during intestine motility. To this end, we proposed a method based on the calculation of the Euclidean distance between the contact surfaces via a contact search method based on k-d-nearest neighbors [40, 41]. When the computed distance falls below a predefined threshold (tol), a penalty force is applied to enforce the separation constraint. This force acts as a repulsive term, proportional to the normal gap, which quantifies the extent of surface penetration. The proposed approach effectively models contact interactions by maintaining a strict separation between surfaces, while promoting robust convergence of the numerical solution.

Remark The proposed method relies on computing the Euclidean distance between surfaces, thereby eliminating the need to assign distinct roles to master and slave surfaces. This makes it particularly well-suited for handling complex contact scenarios, such as self-contact or interactions between multiple bodies.

The goal of this approach is to preserve a minimal positive gap between interacting surfaces by penalizing any violation of the non-interpenetration condition. This ensures accurate contact management, effectively preventing physical overlap between surfaces. Mathematically, the unilateral contact conditions on the two surfaces are given by the following Kuhn-Tucker conditions [65]:

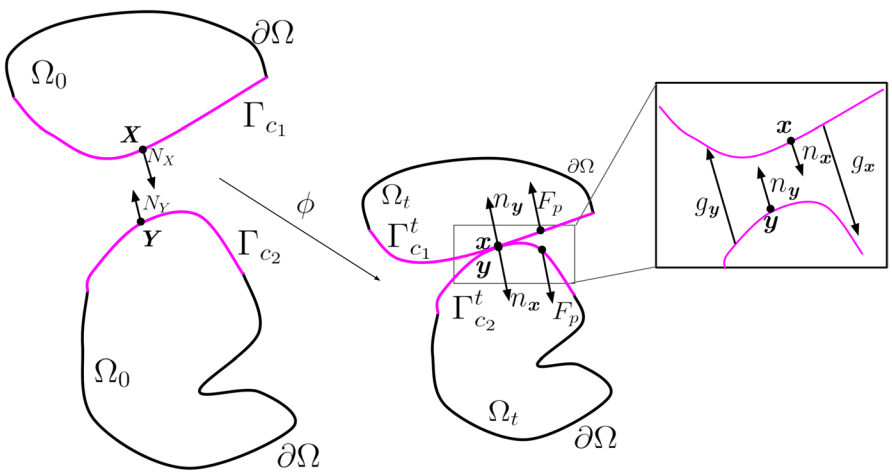

Fig. 2 Concept of contact. $\boldsymbol{X}$ and $\boldsymbol{Y}$ are material points in the reference configuration, while $\boldsymbol{x}$ and $\boldsymbol{y}$ represent their positions in the current configuration. Γ_{c_i} and $\Gamma^t_{c_i}$ are the contact surfaces in the reference and current configurations, respectively, with $i \in 1, 2$. F_p denotes the penalty force applied to both contact surfaces and ϕ is the deformation map. $g_{\boldsymbol{x}}$ and $g_{\boldsymbol{y}}$ are the normal gaps

$$g_x(\boldsymbol{n}_x) = \boldsymbol{u}_x \cdot \boldsymbol{n}_x \geq 0; \quad p_{\boldsymbol{n}_x} = (\boldsymbol{P}\boldsymbol{N}_x) \cdot \boldsymbol{n}_x \leq 0; \\ p_{\boldsymbol{n}_x} g_x(\boldsymbol{n}_x) = 0; \quad \text{on} \quad \Gamma_{c_1}, \tag{8}$$

$$g_y(\boldsymbol{n}_y) = \boldsymbol{u}_y \cdot \boldsymbol{n}_y \geq 0; \quad p_{\boldsymbol{n}_y} = (\boldsymbol{P}\boldsymbol{N}_y) \cdot \boldsymbol{n}_y \leq 0; \\ p_{\boldsymbol{n}_y} g_y(\boldsymbol{n}_y) = 0; \quad \text{on} \quad \Gamma_{c_2}, \tag{9}$$

where, $g_{\boldsymbol{x}}(\boldsymbol{n}_x)$, and $g_{\boldsymbol{y}}(\boldsymbol{n}_y)$ are the normal gaps between two generic points belonging respectively to Γ_{c_1} and to Γ_{c_2} potentially entering in contact, $p_{\boldsymbol{n}_x}$ and $p_{\boldsymbol{n}_y}$ are the normal contact tractions aligned with the normals $\boldsymbol{n}_x$ and $\boldsymbol{n}_y$, respectively, $\boldsymbol{P}$ is the first Piola-Kirchhoff stress tensor, and finally $\boldsymbol{u}_x$ and $\boldsymbol{u}_y$ are the relative displacements of the surfaces Γ_{c_1} and Γ_{c_2} respectively.

One of the simplest ways to automatically ensure the satisfaction of contact inequalities (Eq. 8) to a given tolerance consists of imposing the following penalized condition:

$$p_{\boldsymbol{n}_x} = -K_0 \langle \text{tol} - g_{\boldsymbol{x}}(\boldsymbol{n}_x) \rangle; \quad p_{\boldsymbol{n}_y} = -K_0 \langle \text{tol} - g_{\boldsymbol{y}}(\boldsymbol{n}_y) \rangle, \tag{10}$$

where $\langle \cdot \rangle$ is the Mackauley operator computing the positive part of the gaps with K_0 a large stiffness penalty value.

The contact forces are then computed as:

$$\mathrm{F}_{N_x} = p_{\boldsymbol{n}_x} \boldsymbol{n}_x, \ \mathrm{F}_{N_y} = p_{\boldsymbol{n}_y} \boldsymbol{n}_y. \tag{11}$$

2.4.2 Contact search algorithm based on k-d tree nearest neighbors

Let Γ_{c_1} and Γ_{c_2} denote the two contact surfaces, both belonging to the deformable domain Ω_0. In the reference configuration, the nodal coordinates of these surfaces are extracted from the initial mesh. As the structure undergoes loading, the surfaces deform according to the nodal displacements obtained from solving the mechanical problem. To accurately track the evolution of the gap, the positions of the surface nodes must be continuously updated in the deformed configuration.

An illustrative schematic of the method is given in Fig. 3, and described as follows.

To evaluate the contact gap between points on the surfaces Γ_{c_1} and Γ_{c_2} in the *current configuration*, the nodes of Γ_{c_2} are first embedded in a hierarchical spatial partitioning structure, where each subdomain is recursively split along coordinate axes to form a binary tree. Each leaf node stores a small number of points from Γ_{c_2}. For any given node $\boldsymbol{x} \in \Gamma_{c_1}$, the algorithm descends the tree to locate the leaf that contains the spatial region most likely to contain the closest neighbor to $\boldsymbol{x}$. At each branching point, we choose the child node whose bounding box is closest to $\boldsymbol{x}$, and we recursively evaluate the distance from $\boldsymbol{x}$ to each candidate point in the leaf. As the algorithm ascends back through the tree, it compares the minimum distance found so far with the distance from $\boldsymbol{x}$ to the other subtree's bounding region. If the latter may contain a closer point, it is also explored; otherwise, it is safely discarded. To ensure physical relevance, the search is restricted to a local *zone of influence* around each point $\boldsymbol{x}$. This zone is defined by the condition $\|\boldsymbol{x} - \boldsymbol{y}\| \leq \alpha_{\text{loc}} \cdot d_{\text{loc}}$, where d_{loc} is a local spacing metric and α_{loc} is a scaling factor controlling the extent of the influence region. This ensures that the closest point $\boldsymbol{y}^*(\boldsymbol{x}) \in \Gamma_{c_2}$ lies within a geometrically meaningful neighborhood of $\boldsymbol{x}$, allowing us to define the unsigned contact gap as:

$$g(\boldsymbol{x}) = \min_{\boldsymbol{y} \in \Gamma_{c_2}} \|\boldsymbol{x} - \boldsymbol{y}\|. \tag{12}$$

This result is guaranteed by the algorithm's exhaustive comparison against all subregions that could contain a closer point, ensuring that $\boldsymbol{y}^*(\boldsymbol{x})$ satisfies the validity criterion

$$\|\boldsymbol{x} - \boldsymbol{y}^*(\boldsymbol{x})\| \leq \|\boldsymbol{x} - \boldsymbol{y}\|, \quad \forall \boldsymbol{y} \in \Gamma_{c_2}. \tag{13}$$

To include directional information, the gap is projected along a normalized direction $\boldsymbol{n}_x$, which is computed as the normalized gradient of the scalar distance field, i.e., $\boldsymbol{n}_x = \nabla g(\boldsymbol{x}) / \|\nabla g(\boldsymbol{x})\|$, rather than using geometric normals, which may not be well defined or reliable under large deformations. The normal gap is then defined as:

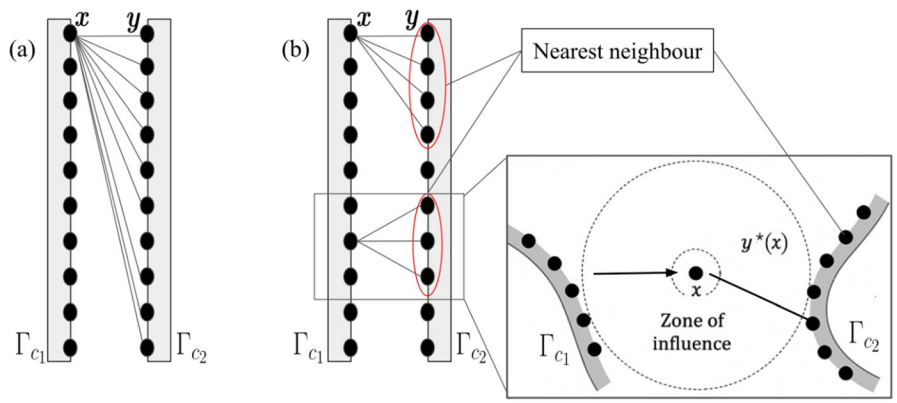

Fig. 3 Concept of contact search based on the nearest neighbor algorithm: $\boldsymbol{x}$ and $\boldsymbol{y}$ represent points on the contact surfaces Γ_{c_1} and Γ_{c_2}, respectively, in the current configuration. Comparison of the method without (a) and with (b) the optimized search method incorporating the nearest neighbor algorithm: $\boldsymbol{y}^*(\boldsymbol{x})$ represents the closest point to $\boldsymbol{x}$ within the zone of influence

$$g_{\boldsymbol{x}}(\boldsymbol{n}_x) = (\boldsymbol{y}^*(\boldsymbol{x}) - \boldsymbol{x}) \cdot \boldsymbol{n}_x. \tag{14}$$

Eq.s 12-14 are used to compute the gap in Eq. 8, the same approach is used to compute the gap $g_{\boldsymbol{y}}(\boldsymbol{n}_y)$.

The contact search algorithm base on k-d tree nearest neighbour is described in Algorithm 1.

Require: A set of points $\Gamma_{c_2} = \{\boldsymbol{y}_1, \boldsymbol{y}_2, \ldots, \boldsymbol{y}_M\}$, a set of query points $\Gamma_{c_1} = \{\boldsymbol{x}_1, \boldsymbol{x}_2, \ldots, \boldsymbol{x}_N\}$.
Ensure: The minimum distance $g(\boldsymbol{x})$ for each $\boldsymbol{x} \in \Gamma_{c_1}$.
1: **Step 1: Build the k-d tree**
2: Construct a k-d tree for the points in Γ_{c_2}. ▷ This organizes the points of Γ_{c_2} into a space-partitioning tree.
3: **Step 2: Initialize Results**
4: Create an empty array $\mathcal{G}$ to store the gap $g(\boldsymbol{x})$ for each $\boldsymbol{x} \in \Gamma_{c_1}$.
5: **Step 3: Perform Nearest Neighbor Search**
6: **for** each point $\boldsymbol{x} \in \Gamma_{c_1}$ **do**
7: Query the k-d tree to find the nearest neighbor $\boldsymbol{y} \in \Gamma_{c_2}$ to $\boldsymbol{x}$.
8: Compute the Euclidean distance: $g(\boldsymbol{x})$
9: Store $g(\boldsymbol{x})$ in $\mathcal{G}$.
10: **end for**
11: **Step 4: Return Results**
12: **return** $\mathcal{G}$, the array of minimum distances.

Algorithm 1 Nearest Neighbor Search Using KD-Tree algorithm

3 Numerical implementation and benchmark test

3.1 Benchmark test: contact between two solids

The contact method is tested against a benchmark problem taken from Wriggers et al. [37]. The problem configuration is explained in Fig. 4. In this benchmark, the upper body is moved downwards in progressive steps to compress the elastic foundation. We model the upper body and the foundation as linear elastic solids with different material properties. The constitutive law for each solid is characterized by the stress–strain relation $\boldsymbol{\sigma} = \lambda \mathrm{tr}(\epsilon)\mathrm{I} + 2\mu\epsilon$, where λ and μ are the Lamé constants and ϵ is the strain tensor. The Young modulus and Poisson ratio are given by $E_u = 7000\ MPa$, $E_f = 70000\ MPa$, $\nu_u = 0.3$, and $\nu_f = 0.45$, where the subscripts 'u' and 'f' stand for the upper body and foundation, respectively. The numerical test is performed using the following weak form for all test functions $\delta\boldsymbol{v}$ belonging to an admissible Sobolev space.

$$\begin{aligned}\mathcal{B}(\boldsymbol{u}; \delta\boldsymbol{v}) := &\int_{\Omega_0} \boldsymbol{\sigma}(\boldsymbol{u}) : \epsilon(\delta\boldsymbol{v})\, \mathrm{d}V \\ &+ \int_{\Gamma_{c_u}} K_0 \langle \mathrm{tol} - g_{c_u} \rangle \boldsymbol{n}_{c_u} \cdot \delta\boldsymbol{v}\, \mathrm{d}\Gamma \\ &+ \int_{\Gamma_{c_f}} K_0 \langle \mathrm{tol} - g_{c_f} \rangle \boldsymbol{n}_{c_f} \cdot \delta\boldsymbol{v}\, \mathrm{d}\Gamma = 0,\end{aligned} \tag{15}$$

In Eq. 15, $\boldsymbol{n}_{c_u}$ and $\boldsymbol{n}_{c_f}$ denote the contact normals, and g_{c_u} and g_{c_f} represent the corresponding contact gaps, computed from the contact boundaries Γ_{c_u} and Γ_{c_f}, respectively. The normal stress distribution obtained with the contact method is reported in Fig. 4. We observe that the method exhibits a violation when the compression is maintained beyond a certain threshold (tol). However, this gap violation appears to be minimally affected by the defined tolerance. The vertical displacement of the foundation against the vertical displacement of the upper body is shown in Fig. 4 as reported in [37]. The results show little variation with respect to the tolerance, demonstrating the robustness of the method.

An additional analysis was performed to assess the computational cost of our algorithm. Specifically, we compared the time required to compute the contact gap in two configurations: with and without the use of nearest neighbor search (NNS). The analysis was carried out as a function of the number of degrees of freedom (DoFs) in the system. As shown in Fig. 4, the incorporation of NNS leads to a substantial reduction in computational time, particularly at higher DoFs. The figure also reports the time-saving percentage per degree of freedom. Notably, for problems with a small number of DoFs, the overhead introduced by the NNS may outweigh its benefits, resulting in a negative time saving. However, as the DoFs increase, the efficiency gain becomes increasingly pronounced, demonstrating the scalability and effectiveness of the NNS-based approach for large-scale problems.

4 Case-study: self-contact in the GI system

4.1 Geometry and weak formulation

The model problem concerns a tract of the intestine geometrically represented as a U-shaped three-dimensional domain, as shown in Fig 5. This configuration has been

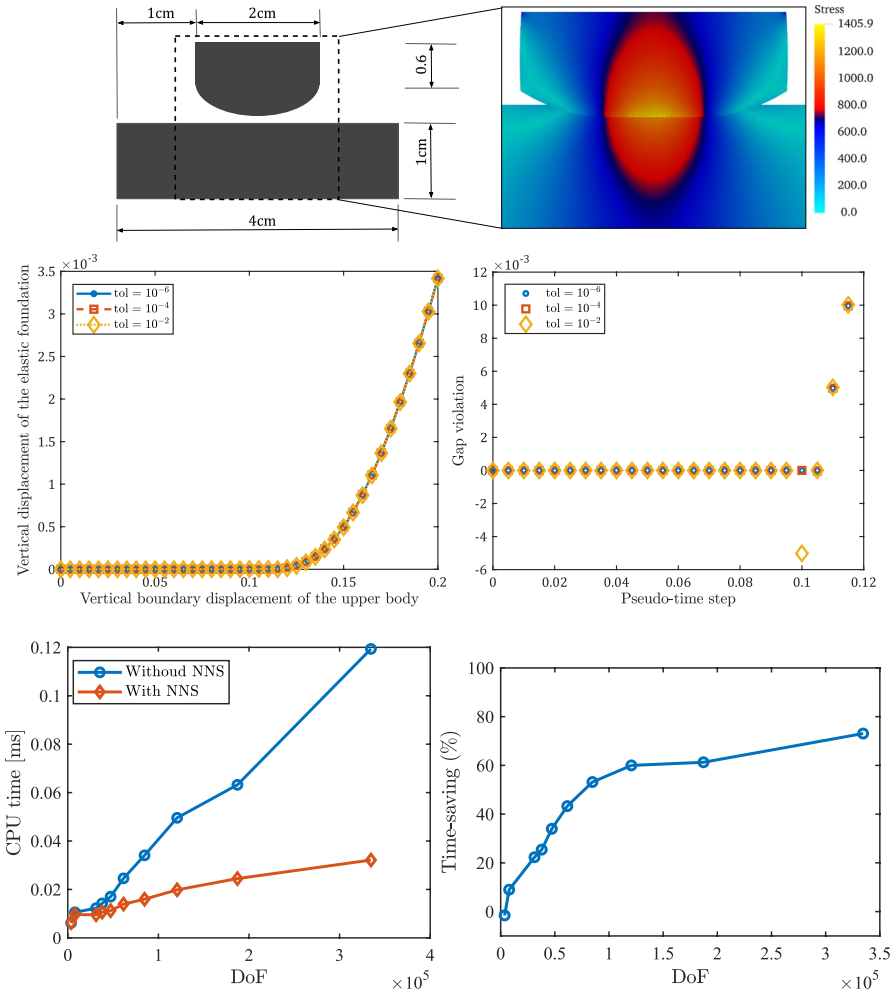

Fig. 4 Benchmark problem of the compression of an elastic body against an elastic foundation. The mesh was refined with a local dimension of 0.03 cm for the two bodies. The zoom plot shows the stress, gap violation and vertical displacement of the plate for the benchmark problem. The two solids are modeled as linear elastic bodies with different material properties: $E_u = 7000$ MPa , $\nu_u = 0.3$, $E_f = 70000$ MPa, $\nu_f = 0.45$. The last two figures represent the computational time with and without the nearest neighbor contact search (NNS) vs. the number of DoFs, and time-saving percentage per degree of freedom

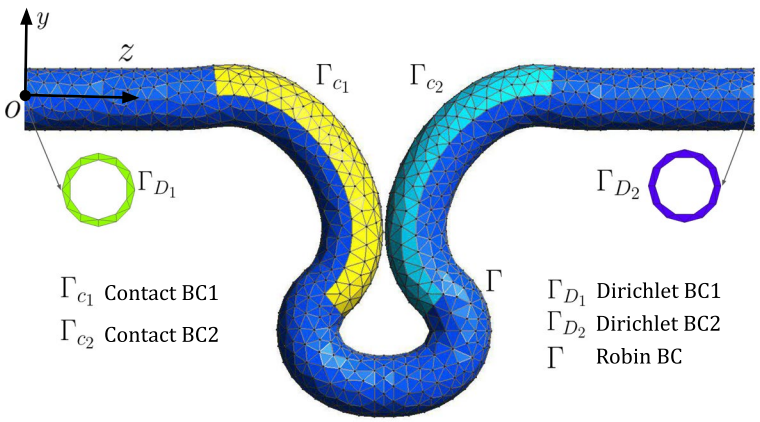

Fig. 5 Problem setting: Γ_{c_1} and Γ_{c_2} are contact surfaces, while Γ, Γ_{D_1}, and Γ_{D_2} are used for Robin and Dirichlet boundary conditions, respectively

chosen to represent a section of the intestine that may come into self-contact during the propagation of the peristaltic wave or due to some pathology causing a dislocation from its physiological configuration.

As illustrated in Fig. 5, the contact surfaces are defined as the inner faces of the structure, highlighted in yellow and cyan, and denoted by Γ_{c_1} and Γ_{c_2}, respectively. The end surfaces, shown in green and violet, correspond to Dirichlet boundary regions (Γ_{D_1}, Γ_{D_2}) and are either fixed or prescribed with a displacement, depending on the specific problem configuration. The remaining boundary, depicted in blue and labeled Γ, is subjected to Robin-type boundary conditions to model the pressure exerted on the intestine by surrounding organs, as discussed in the following section.

As previously mentioned, this work adopts a two-field incompressible formulation to accurately capture soft tissue

mechanics while avoiding volumetric locking. The computational domain is discretized using tetrahedral elements-a choice driven primarily by considerations of numerical stability in the electrophysiological component, which is particularly sensitive to mesh topology. Given that the mechanical formulation is specifically designed to alleviate locking effects, the use of tetrahedral elements offers an effective compromise: it ensures adequate performance for the mechanical model while maintaining high fidelity in the electrophysiological simulation. Although a multi-mesh strategy-employing separate meshes for each physical field with appropriate projection operators-could further optimize performance, this approach is beyond the scope of the present study.

For the problem under consideration, the weak formulation involves finding the displacement field $\boldsymbol{u}$ and the hydrostatic solid pressure p such that:

$$\begin{aligned}\mathcal{M}(\boldsymbol{u}, p; \delta\boldsymbol{u}, \delta p) := &\int_{\Omega_0} \boldsymbol{P} : \nabla\delta\boldsymbol{u} \, \mathrm{d}V \\ &- \int_{\Gamma_N} p_0(t) J\boldsymbol{F}^{-T}\boldsymbol{N} \cdot \delta\boldsymbol{u} \, \mathrm{d}\Gamma \\ &+ \int_{\Omega_0} (J-1)\delta p \, \mathrm{d}V + \int_{\Omega_0} \zeta_{stab} \nabla p \cdot \nabla\delta p \, \mathrm{d}V \\ &+ \int_{\Gamma} J\,\boldsymbol{R}_{\mathrm{rob}} \cdot \boldsymbol{F}^{-T}\boldsymbol{u} \cdot \delta\boldsymbol{u} \, \mathrm{d}\Gamma \\ &+ \int_{\Gamma_{c_1}} K_0 \langle \mathrm{tol} - g_{c_1} \rangle \boldsymbol{n}_{c_1} \cdot \delta\boldsymbol{u} \, \mathrm{d}\Gamma \\ &+ \int_{\Gamma_{c_2}} K_0 \langle \mathrm{tol} - g_{c_2} \rangle \boldsymbol{n}_{c_2} \cdot \delta\boldsymbol{u} \, \mathrm{d}\Gamma = 0,\end{aligned} \tag{16}$$

for all test functions $\delta\boldsymbol{u}$ and δp.

The formulation accounts for a locking-free term ($J - 1 = 0$ in the strong form) to avoid artificial stiffening [68] and the last two terms for the contact forces defined in Eq. (10), which are exerted between the contact surfaces Γ_{c_1} and Γ_{c_2} and are a result of the divergence theorem, where ζ_{stab} is a positive pressure stabilization parameter [69]. The fifth term is a generic form of the Robin boundary condition, which will be customized according to the specific conditions introduced in the following sections. The unknowns were approximated using Lagrangian shape functions, employing $\mathbb{P}_2$ elements for the displacement field and $\mathbb{P}_1$ elements for the pressure field, in order to ensure compliance with the *inf-sup* (Ladyzhenskaya-Babuška-Brezzi) stability condition.

Additionally, the weak form of the electrophysiology problem can be written as it follows: for all test functions $(\delta u_s, \delta v_s, \delta u_i, \delta v_i)$, at each current time step t^{n+1}, and given the solution of the electrophysiology problem at the previous time step $(u_s^n, v_s^n, u_i^n, v_i^n)$ find the vector $(u_s^{n+1}, v_s^{n+1}, u_i^{n+1}, v_i^{n+1})$ such that it is satisfied

$$\begin{aligned}&\int_{\Omega_0} \frac{u_s^{n+1} - u_s^n}{\Delta t}\delta u_s + \int_{\Omega_0} D_s \nabla u_s^{n+1} \cdot \nabla\delta u_s \\ &\quad = \int_{\Omega_0} I_{ion}^s(u_s^n, v_s^n, u_i^n)\delta u_s \,,\end{aligned} \tag{17}$$

$$\int_{\Omega_0} \frac{v_s^{n+1} - v_s^n}{\Delta t}\delta v_s = \int_{\Omega_0} R_s(u_s^n, v_s^n)\delta v_s \,, \tag{18}$$

$$\begin{aligned}&\int_{\Omega_0} \frac{u_i^{n+1} - u_i^n}{\Delta t}\delta u_i \\ &+ \int_{\Omega_0} D_i \nabla u_i^{n+1} \cdot \nabla\delta u_i = \int_{\Omega_0} I_{ion}^i(u_s^n, v_i^n, u_i^n)\delta u_i \,,\end{aligned} \tag{19}$$

$$\int_{\Omega_0} \frac{v_i^{n+1} - v_i^n}{\Delta t}\delta v_i = \int_{\Omega_0} R_i(u_i^n, v_i^n)\delta v_i \,, \tag{20}$$

where:

$$I_{ion}^i(u_s, v_i, u_i) = g(u_i) - v_i + F_i(u_s, u_i) + I_{stim}^i \,, \tag{21}$$

$$R_i(u_i, v_i) = \epsilon_i(z)[\lambda_i(u_i - \beta_i) - v_i] \,, \tag{22}$$

$$I_{ion}^s(u_s, v_s, u_i) = f(u_s) - v_i + F_s(u_s, u_i) \,, \tag{23}$$

$$R_s(u_s, v_s) = \epsilon_s[\lambda_i(u_s - \beta_s) - v_s] \,. \tag{24}$$

We solved the electrophysiology using the monolithic approach before employing the staggered approach (see the "Appendix D") to couple it to the mechanical problem. The residual associated to the monolithic electrophysiological problem is denoted as $\mathcal{E}(u_s, u_i, v_s, v_i; \delta u_s, \delta u_i, \delta v_s, \delta v_i)$.

4.2 Accounting for the mechanical influence of surrounding organs

4.2.1 Distributed boundary stiffness

To account for distributed springs connecting the intestine with the surrounding soft tissues, we impose the following Robin boundary condition (see Fig. 6):

$$\boldsymbol{P}\boldsymbol{N} + \eta(r, z) J\boldsymbol{F}^{-T}\boldsymbol{u} = 0, \quad \text{on } \partial\Omega \times (0, t_{\mathrm{final}}) \tag{25}$$

where, $\boldsymbol{N}$ is the unit normal at the reference configuration and the term $\eta(r, z)$ represents a spatially varying stiffness defined as:

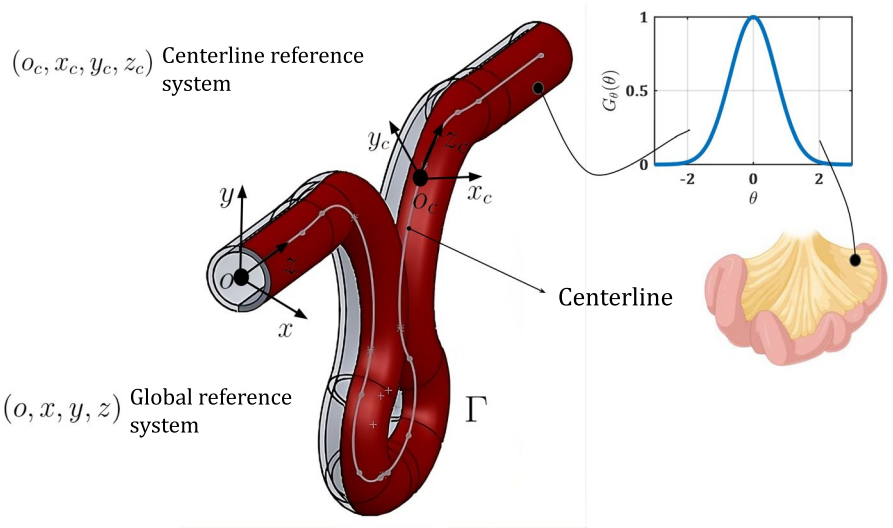

Fig. 6 Schematic of the distribution of the stiffness η on the boundary Γ. The stiffness is distributed along the surface by means of the Gaussian function $G_\theta(\theta)$ linked to the local reference system, $(0_c, x_c, y_c, z_c)$ on the centerline, whereas $(0, x, y, z)$ stands for the global coordinate system

$$\eta(r,s) = \eta_{min} + (\eta_{max} - \eta_{min})\left(1 + \beta\frac{|s - s_{min}|}{|s_{max} - s_{min}|}\right) \exp\left(-\gamma\frac{r - R}{R}\right) G_\theta(\theta), \tag{26}$$

with, $r = \sqrt{(x - x_c(s))^2 + (y - y_c(s))^2}$ the radial distance from the centerline coordinates $(x_c(s), y_c(s))$ and s the curvilinear coordinate; η_{min} and η_{max} are the minimum and maximum stiffness values, respectively; β introduces a stiffness gradient along the z_c-direction; R denotes the mean radius of influence of the surrounding organs on the considered GI tract; γ controls the radial decay of the stiffness coefficient $\eta(r, s)$ around R, such that the stiffness decreases progressively with distance from the mean radius. Finally, $G_\theta(\theta)$ is an azimuthal Gaussian function defined as:

$$G_\theta(\theta) = \begin{cases} \exp\left(-\dfrac{(\theta - \theta_0)^2}{2\sigma^2}\right), & \text{if } |\theta - \theta_0| \leq \frac{\pi}{2}, \\ 0, & \text{else}, \end{cases} \tag{27}$$

where, the azimuthal angle θ is defined as $\theta = \arctan 2(y - y_c(s), x - x_c(s))$; σ stands for the standard deviation and θ_0 is the preferred azimuthal angle.

The spatial distribution of $\eta(r, s)$ considers axial and radial heterogeneities in stiffness, avoiding out-of-plane displacements (see Fig. 15(a)). Such an approach is inspired by [69] and allows us to model several scenarios which will be analyzed in the subsequent sections: (*i*) the mechanical interaction between the digestive tract and its environment (mesentery); (*ii*) the presence of an herniation in a pre-surgical setting; (*iii*) the adhesion syndrome as a result of a post-surgical stiffening and the development of scar bands. From an anatomical perspective, the mesentery is a continuous fold of the peritoneum that suspends the intestine and provides a pathway for blood vessels, lymphatics, and nerves. Structurally, it consists of two layers of serous membrane enclosing connective tissue and fat, within which the vascular and nervous supply is embedded [15, 16]. The mesentery does not envelop the entire intestinal circumference; instead, it typically attaches to only a portion (approximately half) of the wall, most often on the posterior-lateral side. This localized anchoring allows physiological mobility of the bowel while maintaining positional stability (see Fig. 6). The spatially varying stiffness function $\eta(r, s)$ reflects the fact that the mesentery does not uniformly surround the intestine. This non-uniformity is captured by combining a radial exponential decay with a Gaussian distribution in the azimuthal direction. In addition, a longitudinal gradient is introduced to mimic physiological variations along the bowel length. This formulation allows us to represent the compliant yet directionally localized mechanical support provided by the mesentery in a biomechanically and anatomically consistent manner.

Table 1 Parameters for distributed boundaries conditions

$\eta_{\max}$ [kPa/cm]	$\eta_{\min}$ [kPa/cm]	σ [rad]	β [$-$]	γ [$-$]	θ_0 [rad]
0.3	0.1	$\pi/3$	0.5	0.2	0.0

4.2.2 Modeling of the presence of the mesentery

The present case is considered as a reference for a healthy condition. The boundary parameters used to simulate the effect of the mesenteric layer attaching the intestine tract to the posterior abdominal wall are given in Table 1. The numerical analysis was performed maintaining the same electrophysiological and mechanical properties as those used in the case shown in "Appendix B", where no confinement was considered.

When comparing the two cases, due to the lack of any mechano-electric feedback, we observe the same spatio-temporal distribution of membrane potential u_s (see Fig. 7).

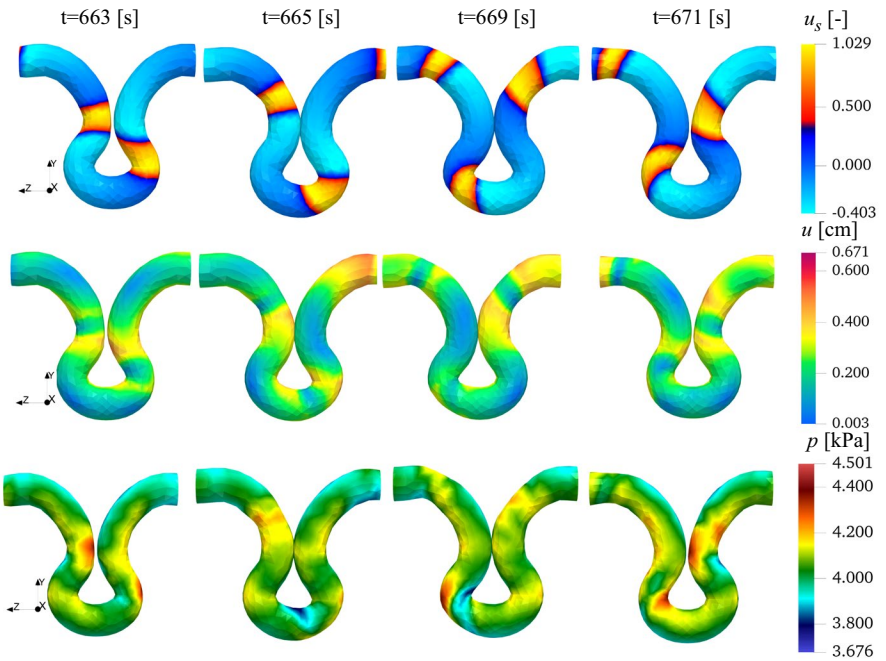

Fig. 7 Temporal evolution of SMC transmembrane voltage u_s, hydrostatic pressure p and displacement u. Electrophysiological and mechanical parameters in Table 2 (Healthy case)

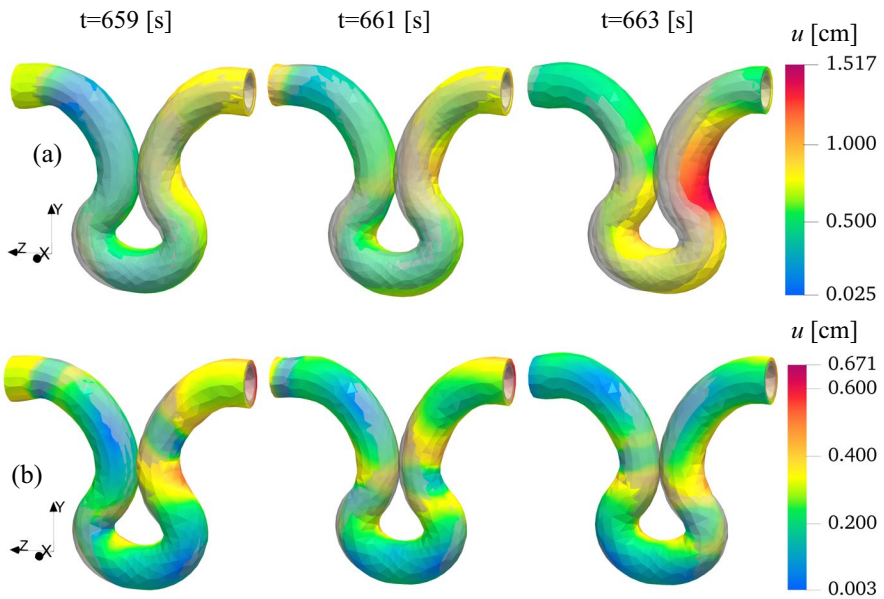

Fig. 8 Effect of the Robin boundary condition. Displacement magnitude $\boldsymbol{u}$**a** without and **b** with the Robin boundary condition applied

However, a notable difference in the global displacement $\boldsymbol{u}$ is obtained. In the unconfined case (Fig. 16) the displacement reaches a maximum of 1.52 cm. In contrast, with the application of the Robin-type condition, the global displacement is reduced by approximately 0.67 cm (see Fig. 7). Pressure distribution curves also show higher values in the unconfined case.

Indeed, without a distributed boundary condition, the intestine moves more freely, leading to increased pressure. To better illustrate our findings, Fig. 8 compares the displacement configurations among the two cases at selected times. The results clearly show that when the intestine is not confined by the presence of other organs, it exhibits significant motility, even in the out of the plane direction, as highlighted in Fig. 8(a). In contrast, when the Robin boundary condition is applied, the domain is stabilized and prevented from moving freely in all directions, as shown in Fig. 8(b).

Figure 9 confirms quantitatively such an observation, showing the displacements in the x- (Fig. 9a) and z- (Fig. 9b) directions. Figure 9c further shows the intraluminal pressure map (manometry patterns) for the distributed boundary case. Regions labeled as 'Geometric pressure' represent constant pressure values induced by the corners of the geometry. Regions labeled 'Contact pressure' are due to the pressure

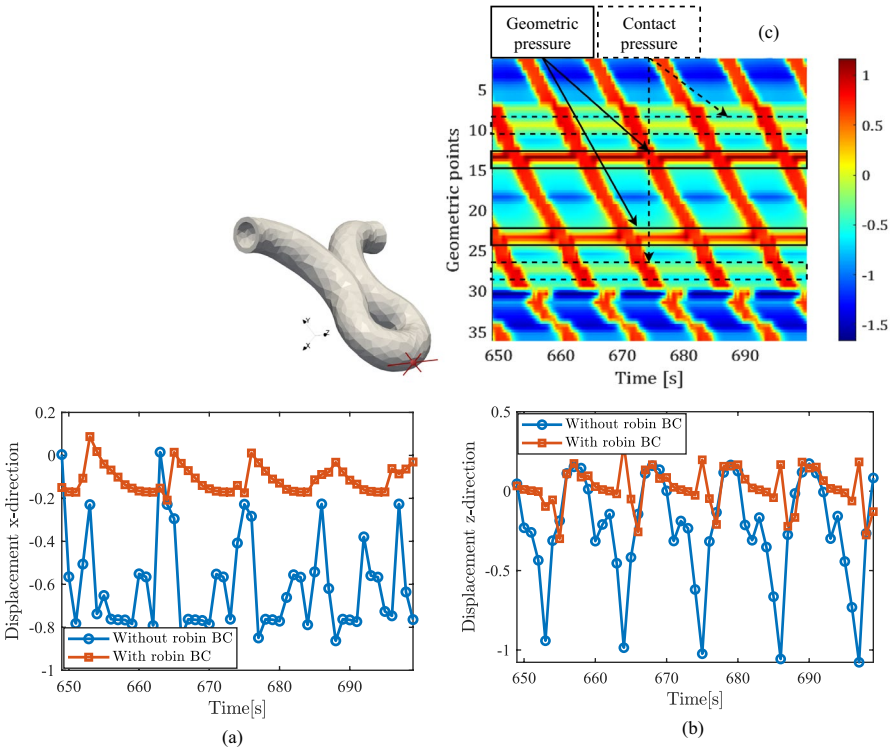

Fig. 9 Comparison of displacement components time course at point $(0, -17, 19.4)$: **a** $x-$direction, **b** $z-$direction and (c) Simulated manometry for the healthy case. The regions labeled as 'Geometric pressure' represent constant pressures induced by the corners of the geometry while the regions labeled 'Contact pressure' are due to the pressure exerted by self-contact. Geometric points (not shown in Fig. 5) refer to 36 points spaced 1 cm apart, extracted from the inner surface of the geometry presented in Fig. 6 along the centerline. Please reader should see in [11] for more details

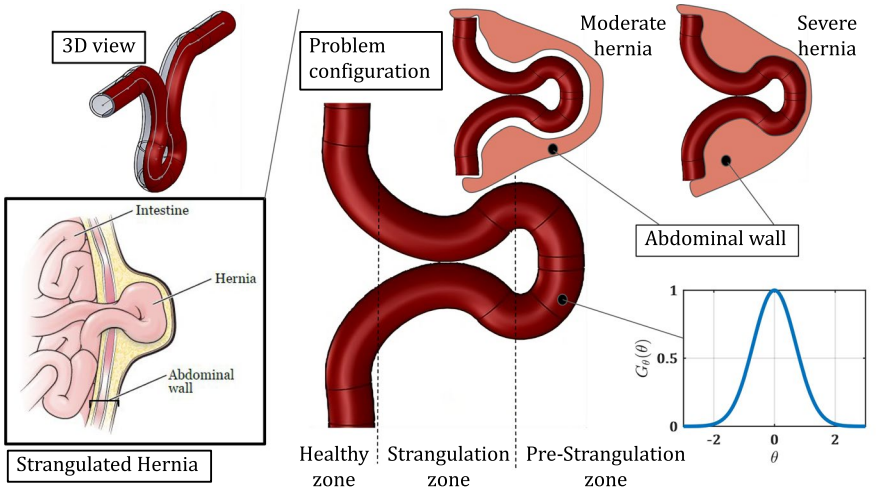

Fig. 10 An abdominal strangulated hernia (picture adapted from [73]). Hernia problem configuration schematics. The mesentery boundary is highlighted in red with associated Gaussian function $G_\theta(\theta)$. Healthy section, strangulation and pre-strangulation zones are identified. Moderate and severe hernia cases are provided on the right

exerted by the self-contact boundary. While these pressures are essential for understanding the structure of the problem, they do not significantly affect the peristaltic motion, as confirmed by the diagonal patterns in Fig. 9c. However, it is worth noting that the model can highlight areas characterized by pressure concentrations and the pressures induced by contact between the intestinal surfaces.

4.3 Modeling strangulation in abdominal hernia

We consider intestinal hernias as a clinical case study (see Fig. 10). Intestinal hernia is a pathological condition in which part of the intestine protrudes through an opening in the abdominal wall or a weakened muscle. Such a condition can occur in a number of anatomical locations, notably in the groin (inguinal hernia) or around the navel (umbilical hernia). Two levels of herniation are considered, moderate and severe [70–72].

The problem configuration is similar to that explained in Sect. 4.2. The area affected by a hernia can be divided into three distinct zones (as shown in Fig. 10), each with specific mechanical properties. In the healthy zone, the intestinal wall retains its physiological elastic characteristics. In the strangulation zone, blood flow is interrupted, leading to ischemia, degradation of cellular structures, and a significant increase in stiffness. Finally, the pre-strangulation

Table 2 Mechanical and Electrophysiological parameters used for Hernia simulation

Mechanical Parameters			
Zones	Healthy	Strangulation	Pre-Strangulation
μ [kPa]	2.5	3	2.7
k_1^l [kPa]	5.14	7	6
k_2^l [−]	1.19	2.1	2
k_1^c [kPa]	0.78	0.9	0.8
k_2^c [−]	0.02	0.04	0.03
k_1^d [kPa]	3.65	4	3.66
k_2^c [−]	0.31	0.35	0.33
Electrophysiological Parameters (Healthy zone)			
SMC layer		**ICC layer**	
$k_s = 10$	$a_s = 0.06$	$k_i = 7$	$a_i = 0.5$
$\beta_s = 0$	$\lambda_s = 8$	$\beta_i = 0.5$	$\lambda_i = 8$
$\epsilon_s = 0.15$	$\alpha_s = 1$	$\epsilon_i = \epsilon_i(z)$	$\alpha_i = -1$
$D_{si} = 0.3$	$D_s = 0.4$	$D_{is} = 0.3$	$D_i = 0.04$

zone is subjected to mechanical stress with possible signs of inflammation and edema, leading to an intermediate stiffness between the healthy zone and the strangulation zone, influenced by fluid accumulation and partial tissue degradation [70, 72, 74]. Simulation parameters are given in Table 2.

Remark In the hernia, for the strangulation zone, the diffusion coefficients $D_s^s = 0.1D_s$ and $D_i^s = 0.1D_i$ and in the pre-strangulation, the diffusion coefficients $D_s^{ps} = 0.5D_s$ and $D_i^{ps} = 0.5D_i$.

In the case of severe intestinal hernia, local variations in electrophysiological properties are observed [72, 75, 76]. The healthy zone, away from the compression, retains physiological behavior with intact conductivity. The pre-strangulation zone undergoes mechanical stress and partial impairment of blood perfusion, resulting in mild inflammation and edema. These effects locally increase the electrical resistance, modeled by a moderate reduction in the diffusion coefficient. Finally, the strangulation zone is marked by severe ischemia and cellular necrosis. This region is modeled by a drastic decrease in the diffusion coefficient, representing a significant reduction in the conduction capacity of electrical signals.

Simulation results for moderate strangulation are provided in "Appendix C": the electrical wave propagates without significant constraints, allowing almost physiological intestine contraction in the strangulation and pre-strangulation zones. The overall motility of the healthy zone is maintained, thus remaining functional. However, in the case of severe strangulation, Fig. 11, a marked slowing of the electrical wave is observed in the strangulation and pre-strangulation zones, leading to a significant reduction in contraction rate and associated motility.

Manometric measurements in strangulation hernias are technically impossible to perform in clinical conditions due to the severe compression of the intestinal lumen that prevents catheter passage. In our self-contact computational framework, intraluminal pressure levels can be analyzed for the first time. In the case of moderate strangulation, Fig. 12(a), the numerically predicted manometric curves showed active contraction in the pre-strangulation zone, constant pressure in the strangulation zone (attributed to pressure exerted by contact surfaces), and persistent physiological contraction in the healthy zones. On the other hand, in the case of severe strangulation, Fig. 12(b), the curves

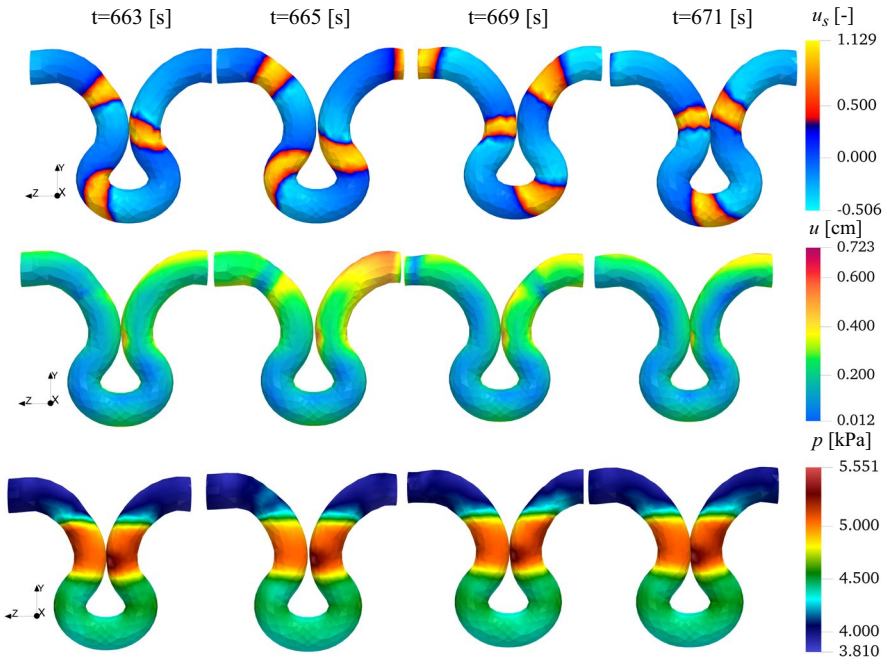

Fig. 11 Temporal evolution of SMC transmembrane voltage u_s, hydrostatic pressure p and displacement u for the severe hernia case

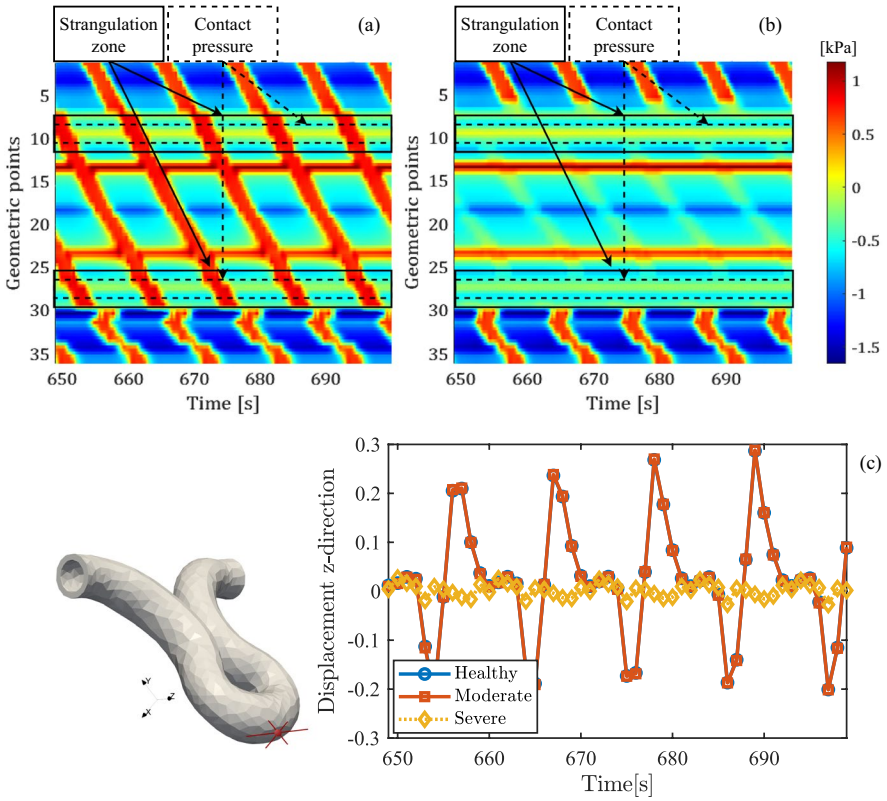

Fig. 12 Simulated manometry for **a** moderate and **b** severe hernia cases. Contractions are absent in the strangulated region of the severe case. **c** Time evolution of z-displacement at point $(0,\ -17,\ 19.4)$ for healthy, moderate, and severe configurations

also revealed a constant contact pressure in the strangulation zone and absence of contraction due to the contact surfaces, associated with negligible contraction in the pre-strangulation zone. It is worth noting that, in the severe case, the constant pressure is more pronounced than in the moderate case. Such a high stress is due to the additional load exerted by the abdomen, acting as an external constraint.

To better understand the underlying phenomena, Fig. 12(c) illustrates the displacement in the z-direction within the pre-strangulation zone for three scenarios: healthy, moderate hernia, and severe hernia. For the moderate hernia case, the displacement closely resembles the healthy case, suggesting the onset of a hernia or a very mild condition. On the other hand, in the case of severe hernia, the computed displacement is significantly smaller despite muscle contraction responding to electrical activation. Such a lack of motility can be attributed to the portion of the intestine that has passed through and is constrained by the abdomen.

4.4 Modeling intestinal adhesion syndrome

One potential application of our model is the study of intestinal adhesion syndrome [18], a common condition that arises after surgical interventions or abdominal inflammations. This syndrome is characterized by the formation of fibrous bands, known as adherents, which connect different parts of the intestine or adjacent organs. These adhesions can lead to severe complications such as chronic pain, intestinal obstructions, and impaired intestinal motility [77, 78].

To investigate this phenomenon without directly modeling the adhesions themselves, we based our study on the geometry shown in Fig. 13(a). From this configuration, we aimed to simulate the restrictive effects of adhesions by introducing specialized boundary conditions as show in Eq. 28.

$$\begin{aligned} &\boldsymbol{PN} + \eta(r,z) J\boldsymbol{F}^{-T}\boldsymbol{u} + \eta_a J\boldsymbol{F}^{-T}(\boldsymbol{u}-\boldsymbol{u}_{ref}) = 0, \\ &\text{on } \partial\Omega \times (0, t_{\text{final}}). \end{aligned} \tag{28}$$

Here, η_a stands for the adherence stiffness (see Fig. 15(b)) while $\boldsymbol{u}_{ref}$ is the initial displacement of the intestinal wall. This approach involves adding a mechanical constraint that replicates the impact of adhesions on displacements and forces. Through this method, we can examine how local restrictions influence intestinal dynamics while maintaining a general electromechanical framework. Material stiffness changes according to Table 3 and the electrophysiology parameter for the healthy case are in the Table 2.

Remark For the Adhesion, the diffusion coefficients are $D_s^a = 0.125 D_s$ and $D_i^a = 0.125 D_i$ in the adhesion region.

For this last test case, we present only the pressure maps in Fig. 13b, c, comparing them with the results from Fig. 7, where adhesion was not considered. At $t = 668$ s, in both

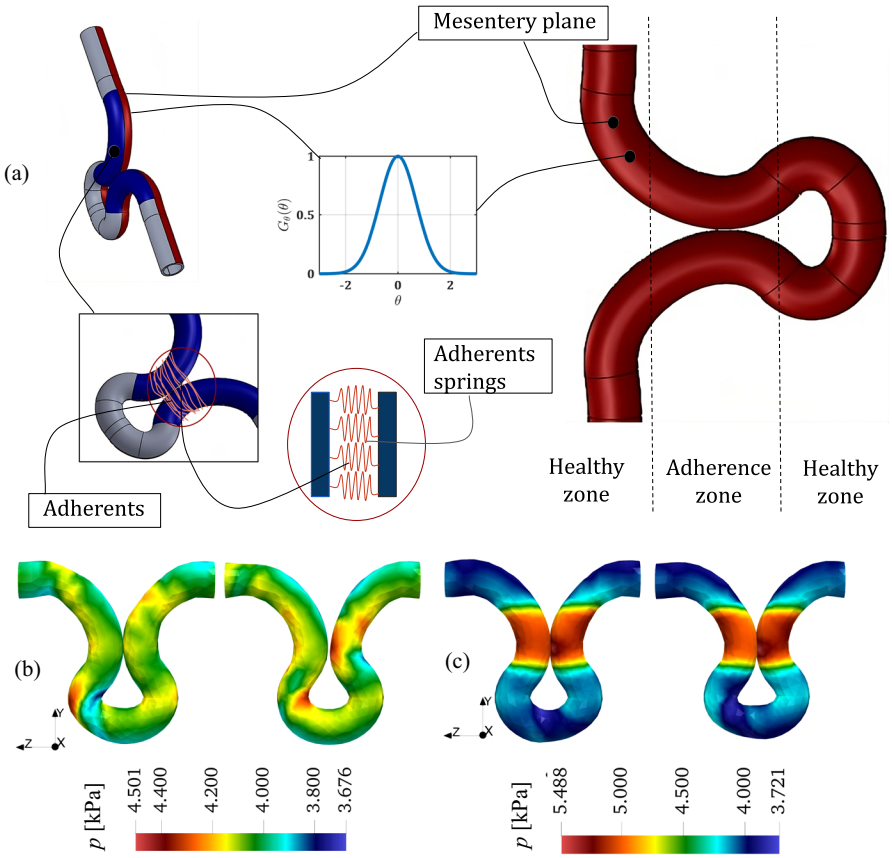

Fig. 13 **a** Schematics of the adhesion problem configuration. The mesentery surface is highlighted in red, along with the associated Gaussian distribution of stiffness. Adherents are modeled as distributed springs along the blue boundary. Temporal evolution of the hydrostatic pressure p in the case of severe intestinal adhesion syndrome: **b** without adhesion, and **c** with adhesion, where the material stiffness has been modified in the adhesion region ($\eta_a = 0.9\,\mathrm{kPa/cm}$, $\boldsymbol{u}_{ref} = 0$). Electrophysiological parameters can be found in Table 2

Table 3 Mechanical constitutive parameters for adhesion syndrome simulation

Zones	Healthy	Adherence
μ [kPa]	2.5	3.1
k_1^l [kPa]	5.14	7
k_2^l [–]	1.19	2.1
k_1^c [kPa]	0.78	0.8
k_2^c [–]	0.02	0.04
k_1^d [kPa]	3.65	4
k_2^c [–]	0.31	0.35

cases, self-contact is observed. However, at $t = 671$ s, a clear difference emerges: in the scenario without adhesion, the intestinal surfaces separate due to the peristaltic wave, while in the case with adhesion, the surfaces remain in contact. Such a condition is further confirmed in Fig. 14b showing the average absolute displacement between two points located at the adherence region. The absolute displacement is reduced then adhesions are present. Reduced motility is also observed on the manometry curves in Fig. 14a. In particular, instead of contraction waves, a slight constant pressure appears, indicating the force exerted by the adhesion, forcing the intestinal walls to remain in contact.

To further investigate this condition, we examined the behavior beyond the adhesion zone. Figure 14c1 and c2 display the displacement and action potential at a point located after the adhesion zone. We observe that the action potential is delayed in the case with adhesion, which consequently slows down the contraction speed. However, this does not systematically affect the displacement amplitude. These findings are in perfect agreement with the manometry results.

5 Conclusions

The study proposed a comprehensive multiphysics framework for modeling intestinal motility, integrating active strain electromechanics, tissue anisotropy, cellular electrophysiology, and self-contact extending and generalizing previous works from the authors [11]. The contact method developed is based on distance computation between contact surfaces employing a penalty force to prevent penetration. The contact method developed is based on distance computation between contact surfaces and, to reduce the computational time for the evaluation of the gap between contact surfaces, an enhanced search method based on the nearest-neighbor algorithm was implemented. Considering

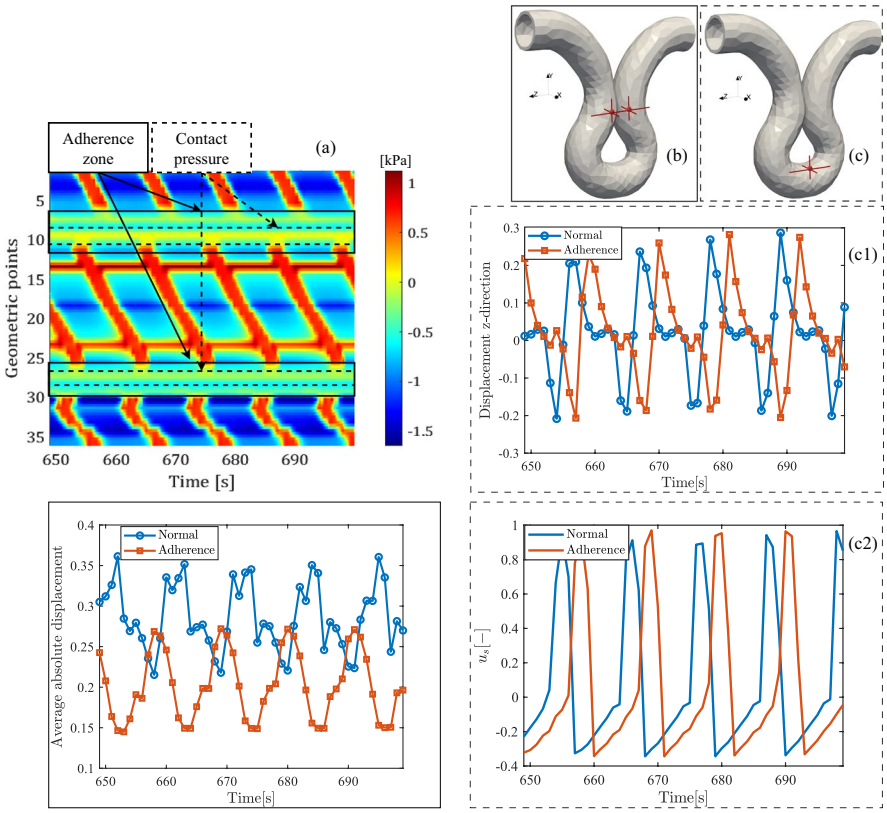

Fig. 14 **a** Simulated manometry in the region affected by the adhesion syndrome. No contractions are observed within the adhesion zone. The area labeled Contact pressure indicates pressure levels resulting from self-contact of tissue surfaces. **b** Absolute displacement between two points located within the adhesion region. **c** Comparison between displacement and smooth muscle membrane potential at the point with coordinates $(1.40,\ -14.1,\ 18.9)$ after adherence zone: **c1** membrane potential u_s in the x-direction, **c2** displacement u in the z-direction

the lubricated conditions, the frictionless contact problem is examined and the unilateral contact conditions are approximately enforced by using the penalty approach. The method was validated using a benchmark test, quantifying the gap violations at the contact interface. Results demonstrated minimal gap violations, showcasing the robustness of the approach. The governing equations were discretized using the finite element method, and a custom code leveraging on `FEniCS` was developed for their resolution.

We exploited the model to study the influence of surrounding organs on intestinal motility. For this purpose, a specialized boundary condition was developed, incorporating a progressive stiffness distribution for external organs (e.g., the mesentery) combined with Gaussian functions. Results indicated that these conditions play a critical role in constraining intestinal motion, preventing free movement. Finally, we investigated two pathological conditions: abdominal hernia and abdominal adhesion (post surgical situation). Although reproducing manometry in such pathological conditions is challenging to implement in clinical practice, our model allowed us to simulate manometric curves in these different pathological scenarios, demonstrating its potential as a predictive tool for clinical applications.

This work investigated the in silico prediction of intestinal electromechanical motility in curved three-dimensional geometries susceptible to self-contact for the first time. Demonstrated model predictability enables several applications in a clinical scenario.

5.1 Limitations and perspectives

Model limitations are herein briefly mentioned. The implemented electrophysiological model can reproduce one type of excitation wave at a time, either slow waves or spikes. Moreover, action potential propagation is unidirectional (aboral direction) not considering the enteric nervous system [13, 79, 80]. The mesentery was reproduced by introducing a Robin-type boundary condition with a spatial distribution of stiffness. Advanced modeling approaches will require porous interfaces enabling multiphysics flux exchanges with the surrounding organs [81, 82]. From a numerical perspective, a contact formulation based on the penalty method can become unstable if the penalty parameter is not properly chosen. As future development, we plan to introduce an adaptive penalty coefficient to enhance model robustness for large scale numerical analyses [39, 45].

Distribution of the stiffness for Robin BC used in all simulations

This section illustrates the distribution of stiffness $\eta(r, s)$ across a surface of the geometry and the additional stiffness η_a, which accounts for the effects of adhesions. Since the stiffness $\eta(r, s)$ represents the influence of the mesentery, it was included in all simulations. On top of this baseline

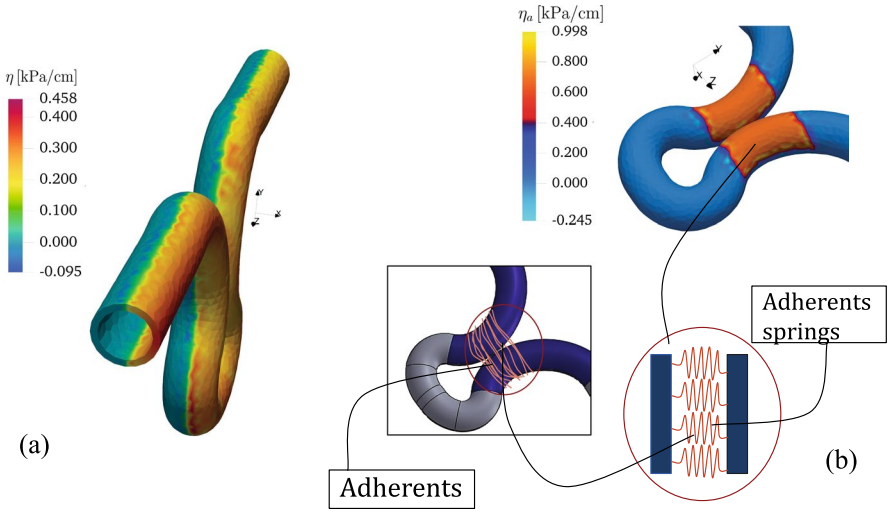

Fig. 15 **a** Distribution of the stiffness η representing the effect of mesentery and **b** show the distribution of the stiffness η_a showing the effect of the adherents

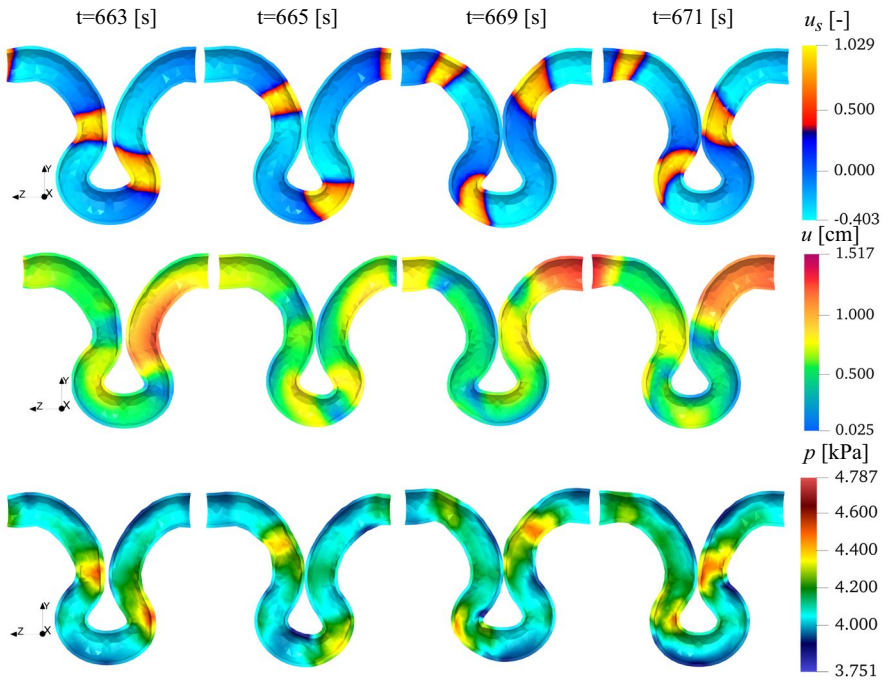

Fig. 16 Temporal evolution of SMC transmembrane voltage u_s, of hydrostatic pressure p and the displacement u for the Euclidean distance method

stiffness, an additional stiffness was introduced solely in the presence of adhesions to simulate the case of the adhesion syndrome.

Application to the problem setting

After testing our contact code on the benchmark problem (see Fig. 4), we proceeded to integrate the contact code into the full electromechanical framework and solved the problem on the geometry described in Fig. 5 using the mechanical problem explained in Eq. 16.

We observe in Fig. 16 that the contact code effectively prevents interpenetration between the contact surfaces. This is particularly evident in the pressure curves, which show an increase in pressure at the contact regions when the surfaces come into contact, notably at t=667 s and t=669 s. This confirms that the contact between the two surfaces is successfully handled by the implemented code.This result was used as a reference for the rest of the simulation

Result for the moderate Hernia

See Fig. 17.

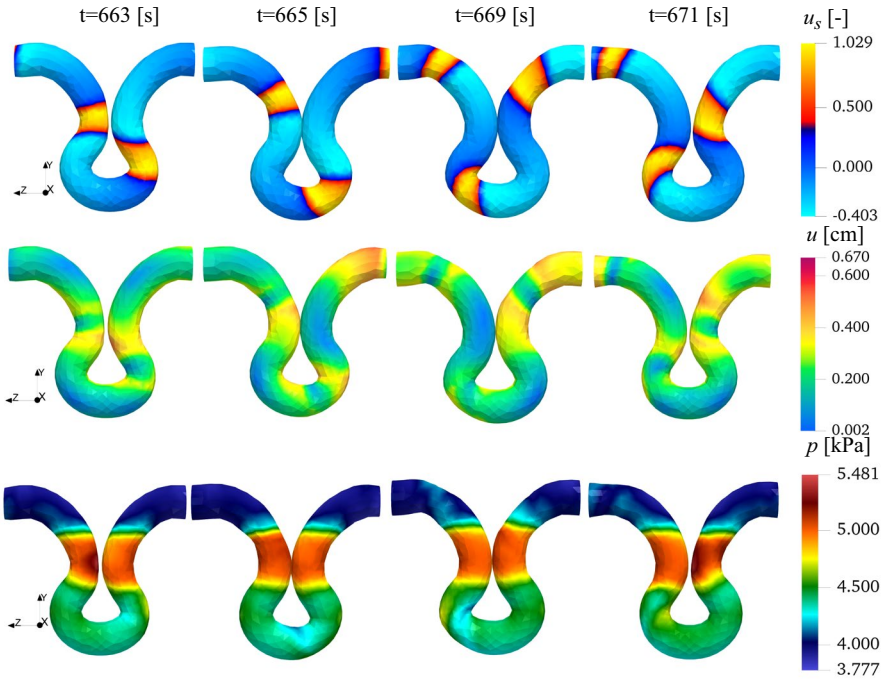

Fig. 17 Temporal evolution of SMC transmembrane voltage u_s, hydrostatic pressure p and displacement u for the moderate hernia case. Electrophysiological parameters are in 2

Staggered algorithm used in the paper

Input Initial and boundary conditions for displacement, pressure and electrophysiological variables:
while $t^n < T$ **do**
  Given: displacement and pressure $\boldsymbol{u}^n, p^n$ solve the linear electrophysiology problem: $\mathcal{E}(u_s^{n+1}, u_i^{n+1}, v_s^{n+1}, v_i^{n+1}; \delta u_s, \delta u_i, \delta v_s, \delta v_i) = 0$
  Update EP solutions $(u_s^n, u_i^n, v_s^n, v_i^n) \leftarrow (u_s^{n+1}, u_i^{n+1}, v_s^{n+1}, v_i^{n+1})$
  Given: the electrophysiological variables $(u_s^{n+1}, u_i^{n+1}, v_s^{n+1}, v_i^{n+1})$, solve the mechanical self-contact problem.
  Contact detection: Run Algorithm. 1
  if Eq. 4 **then** activate contact force
  else Pass
  end if
  Newton-Raphson procedure:
  for a given Newton iteration k **do**
    Given: $\boldsymbol{u}_k^{n+1}$ and p_k^{n+1} solve the linearized mechanical problem: $d\mathcal{M}(\Delta\boldsymbol{u}, \Delta p; \delta\boldsymbol{u}, \delta p) = -\mathcal{M}(\boldsymbol{u}_k^{n+1}, p_k^{n+1}; \delta\boldsymbol{u}, \delta p)$
    Set: $\boldsymbol{u}_{k+1}^{n+1} = \Delta\boldsymbol{u} + \boldsymbol{u}_k^{n+1}$ and $p_{k+1}^{n+1} = \Delta p + p_k^{n+1}$
    if $\|\boldsymbol{u}_{k+1}^{n+1} - \boldsymbol{u}_k^{n+1}\| < tol$ **then**
      Update the Newton solutions $\boldsymbol{u}_k^{n+1} \leftarrow \boldsymbol{u}_{k+1}^{n+1}$ and $p_k^{n+1} \leftarrow p_{k+1}^{n+1}$
    else $k \leftarrow k + 1$
    end if
    Update mechanical solutions $\boldsymbol{u}^{n+1} \leftarrow \boldsymbol{u}_{k+1}^{n+1}$ and $p^{n+1} \leftarrow p_{k+1}^{n+1}$
  end for
  Update time: $t \leftarrow t + \Delta t$
  Output: Displacement $\boldsymbol{u}^{n+1}$, pressure p^{n+1} and electrophysiological variables $(u_s^{n+1}, v_s^{n+1}, u_i^{n+1}, v_i^{n+1})$ at the current time t^{n+1}
end while

Algorithm 2 Algorithm for the electromechanical motility with self-contact

Acknowledgements Authors acknowledge the support of the Italian National Group for Mathematical Physics (GNFM-INdAM) and the ERC Consolidator Grant MiGEM #101170592, CUP C83C25000140006.

Funding Open access funding provided by Scuola IMT Alti Studi Lucca within the CRUI-CARE Agreement.

Data Availability All the data utilized are detailed within this article and the code will be made available upon request.

Declarations

Conflict of interest Nothing to declare.

References

1. Azzouz LL, Sharma S (2018) Physiology. Large Intestine. StatPearls Publishing, Treasure Island (FL)
2. Sulaiman S, Marciani L (2019) MRI of the colon in the pharmaceutical field: the future before us. Pharmaceutics 11(4):146
3. Precup G, Vodnar D-C (2019) Gut prevotella as a possible biomarker of diet and its eubiotic versus dysbiotic roles: a comprehensive literature review. Br J Surg 122(2):131–140
4. Aliev RR, Richards W, Wikswo JP (2000) A simple nonlinear model of electrical activity in the intestine. J Theor Biol 204(1):21–28
5. Sharon Y, Nisky I (2018) Expertise, teleoperation, and task constraints affect the speed-curvature-torsion power law in ramis. J Med Robot Res 3(03n04):1841008
6. Du P, Calder S, Angeli TR, Sathar S, Paskaranandavadivel N, O'Grady G, Cheng LK (2018) Progress in mathematical modeling of gastrointestinal slow wave abnormalities. Front Physiol 8:1136
7. Nagaraja S, Leichsenring K, Ambati M, De Lorenzis L, Böl M (2021) On a phase-field approach to model fracture of small intestine walls. Acta Biomater 130:317–331
8. Sokolis DP, Sassani SG (2013) Microstructure-based constitutive modeling for the large intestine validated by histological observations. J Mech Behav Biomed Mater 21:149–166
9. Brandstaeter S, Gizzi A, Fuchs SL, Gebauer AM, Aydin RC, Cyron CJ (2018) Computational model of gastric motility with active-strain electromechanics. ZAMM J Appl Math Mech 98(12):2177–2197
10. Du P, Lim J, Cheng LK (2013) A model of electromechanical coupling in the small intestine. Multiscale Comput Model Biomech Biomed Eng. pp 179–207
11. Djoumessi RT, Lenarda P, Gizzi A, Giusti S, Alduini P, Paggi M (2024) In silico model of colon electromechanics for manometry prediction after laser tissue soldering. Comput Methods Appl Mech Eng 426:116989
12. Patton HN, Zhang H, Wood GA, Guragain B, Nagahawatte ND, Nisbet LA, Cheng LK, Walcott GP, Rogers JM (2024) Simultaneous optical imaging of gastric slow waves and contractions in the in vivo porcine stomach. Am J Physiol Gastrointest Liver Physiol 327(6):765–782
13. Athavale ON, Di Natale MR, Avci R, Clark AR, Furness JB, Cheng LK, Du P (2024) Mapping the rat gastric slow-wave conduction pathway: bridging in vitro and in vivo methods, revealing a loosely coupled region in the distal stomach. Am J Physiol Gastrointest Liver Physiol 327(2):254–266
14. Kuruppu S, Cheng LK, Angeli-Gordon TR, Avci R, Paskaranandavadivel N (2024) Electromechanical response of mesenteric ischemia defined through simultaneous high-resolution bioelectrical and video mapping. Ann Biomed Eng 52(3):588–599
15. Byrnes KG, Walsh D, Dockery P, McDermott K, Coffey JC (2019) Anatomy of the mesentery: Current understanding and mechanisms of attachment. In: Seminars in Cell & Developmental Biology, vol. 92, pp. 12–17. Elsevier
16. Sensoy I (2021) A review on the food digestion in the digestive tract and the used in vitro models. Curr Res Food Sci 4:308–319
17. Pfaller MR, Hörmann J, Weigl M, Nagler A, Chabiniok R, Bertoglio C, WA W (2019) The importance of the pericardium for cardiac biomechanics: from physiology to computational modeling. Biomech Model Mechanobiol 18(2):503–529
18. Tabibian N, Swehli E, Boyd A, Umbreen A, Tabibian J (2017) Abdominal adhesions: a practical review of an often overlooked entity. Ann Med Surg 15:9–13
19. Frager D, Baer JW, Medwid SW, Rothpearl A, Bossart P (1996) Detection of intestinal ischemia in patients with acute small-bowel obstruction due to adhesions or hernia: efficacy of ct. AJR Am J Roentgenol 166(1):67–71
20. Cardoz AV, Kumar RR, Banerjee N, Kumar SR (2024) Acute intestinal obstruction due to obturator hernia: a case series. Cureus 16(4)
21. Furtado T, Carvalho A, Garcia D (2024) Estrangulated obturatory hernia. case report of a challenging diagnosis of obstructive syndrome. Int J Surg Case Rep 118:109643
22. Jadhav GS, Adhikari GR, Purohit RS (2022) A prospective observational study of ventral hernia. Cureus **14**(8)
23. Moazzez A, Dubina E, Park H, Shover A, Kim D, Virgilio C (2021) Outcomes of concomitant mesh placement and intestinal procedures during open ventral hernia repair. Hernia 25:701–708
24. Klifto K, Othman S, Messa C, Piwnica-Worms W, Fischer J, Kovach S (2021) Risk factors, outcomes, and complications associated with combined ventral hernia and enterocutaneous fistula single-staged abdominal wall reconstruction. Hernia, 1–12
25. Akbaba S, Atila D, Keskin D, Tezcaner T, Tezcaner A (2021) Multilayer fibroin/chitosan oligosaccharide lactate and pullulan immunomodulatory patch for treatment of hernia and prevention of intraperitoneal adhesion. Carbohydr Polym 265:118066
26. Chouly F, Hild P, Renard Y (2023) Finite element approximation of contact and friction in elasticity. Springer, Cham
27. Li B, Li P, Zhou R, Feng X-Q, Zhou K (2022) Contact mechanics in tribological and contact damage-related problems: A review. Tribol Int 171:107534
28. Areias P, Sukumar N, Ambrósio J (2023) Continuous gap contact formulation based on the screened poisson equation. Comput Mech 72(4):707–723
29. Pore T, Thorat SG, Nema AA (2021) Review of contact modelling in nonlinear finite element analysis. Mater Today Proc 47:2436–2440

30. Bozorgmehri B, Yu X, Matikainen MK, Harish AB, Mikkola A (2021) A study of contact methods in the application of large deformation dynamics in self-contact beam. Nonlinear Dyn 103:581–616
31. Xuan L, Yan C, Gong J, Li C, Li H (2024) A penalty-based cell vertex finite volume method for two-dimensional contact problems. Comput Mech 1–16
32. Paggi M, Zavarise G (2011) Contact mechanics of microscopically rough surfaces with graded elasticity. Euro J Mech A/Solids 30(5):696–704
33. Paggi M, Bemporad A, Reinoso J (2020) Computational methods for contact problems with roughness. Model Simulat Tribol Problem Technol, pp 131–178
34. Zavarise G, Wriggers P, Schrefler B (1998) A method for solving contact problems. Int J Numer Methods Eng 42(3):473–498
35. Chouly F, Mlika R, Renard Y (2018) An unbiased nitsche s approximation of the frictional contact between two elastic structures. Numer Math 139:593–631
36. Lorez F, Pundir M, Kammer DS (2024) Eulerian framework for contact between solids represented as phase fields. Comput Methods Appl Mech Eng 418:116497
37. Wriggers P, Schröder J, Schwarz A (2013) A finite element method for contact using a third medium. Comput Mech 52:837–847
38. Wriggers P, Korelc J, Junker P (2025) A third medium approach for contact using first and second order finite elements. Comput Methods Appl Mech Eng 436:117740
39. Frederiksen AH, Dalklint A, Sigmund O, Poulios K (2025) Improved third medium formulation for 3d topology optimization with contact. Comput Methods Appl Mech Eng 436:117595
40. Hou W, Li D, Xu C, Zhang H, Li T (2018) An advanced k nearest neighbor classification algorithm based on kd-tree. In: 2018 IEEE international conference of safety produce informatization (IICSPI), pp 902–905. IEEE
41. Kamaludin S, Thamburaja P (2023) Efficient neighbour search algorithm for nonlocal-based simulations application to failure mechanics. J Fail Anal Prev 23(2):540–547
42. Lowe DG (2004) Distinctive image features from scale-invariant keypoints. Int J Comput Vis 60:91–110
43. Ram P, Sinha K (2019) Revisiting kd-tree for nearest neighbor search. In: Proceedings of the 25th ACM Sigkdd international conference on knowledge discovery & data mining, pp 1378–1388
44. Sharma S, Buist ML (2025) A comparative study of constitutive relations and variational formulations for modeling gastrointestinal peristalsis. J Mech Behav Biomed Mater 168:107013
45. Poulios K, Renard Y (2015) An unconstrained integral approximation of large sliding frictional contact between deformable solids. Comput Struct 153:75–90
46. Mlika R, Renard Y, Chouly F (2017) An unbiased nitsche s formulation of large deformation frictional contact and self-contact. Comput Methods Appl Mech Eng 325:265–288
47. Nan Z, Fang Y, Yang P, Meng S, Zhou J, Liu B (2023) Strong-anisotropy-induced instability and discussion on kink band under complex loads. Ext Mech Lett 62:102043
48. Han W, Wang S, Liu W, Sun W, Hou Q (2024) Nonlinear nmm analysis for large deformation and contact problems: Using full strain-rotation decomposition algorithm and augmented lagrangian method enhanced open-closed iteration. Eng Anal Bound Elem 169:105971
49. Holzapfel GA (2002) Nonlinear solid mechanics: a continuum approach for engineering science. Meccanica 37(4):489–490
50. Cherubini C, Filippi S, Nardinocchi P, Teresi L (2008) An electromechanical model of cardiac tissue: constitutive issues and electrophysiological effects. Prog Biophys Mol Biol 97(2–3):562–573
51. Ambrosi D, Arioli G, Nobile F, Quarteroni A (2011) Electromechanical coupling in cardiac dynamics: the active strain approach. SIAM J Appl Math 71(2):605–621
52. Huizinga JD, Lammers WJ (2009) Gut peristalsis is governed by a multitude of cooperating mechanisms. Am J Physiol Gastrointest Liver Physiol 296(1):1–8
53. Sanders KM, Kito Y, Hwang SJ, Ward SM (2016) Regulation of gastrointestinal smooth muscle function by interstitial cells. Physiology 31(5):316–326
54. Sanders KM, Koh SD, Ward SM (2006) Interstitial cells of cajal as pacemakers in the gastrointestinal tract. Annu Rev Physiol 68:307–343
55. Corrias A, Buist ML (2007) A quantitative model of gastric smooth muscle cellular activation. Ann Biomed Eng 35:1595–1607
56. Corrias A, Buist ML (2008) Quantitative cellular description of gastric slow wave activity. Am J Physiol Gastrointest Liver Physiol 294(4):989–995
57. Hanani M, Farrugia G, Komuro T (2005) Intercellular coupling of interstitial cells of cajal in the digestive tract. Int Rev Cytol 242:249–282
58. Gizzi A, Cherubini C, Migliori S, Alloni R, Portuesi R, Filippi S (2010) On the electrical intestine turbulence induced by temperature changes. Phys Biol 7(1):016011
59. Sokolis DP (2021) Variation of passive biomechanical properties of the small intestine along its length: microstructure-based characterization. Bioengineering 8(3):32
60. Patel B, Gizzi A, Hashemi J, Awakeem Y, Gregersen H, Kassab G (2022) Biomechanical constitutive modeling of the gastrointestinal tissues: a systematic review. Mater Des 217:110576
61. Popp A, Gee MW, Wall WA (2009) A finite deformation mortar contact formulation using a primal-dual active set strategy. Int J Numer Meth Eng 79(11):1354–1391
62. Popp A, Gitterle M, Gee MW, Wall WA (2010) A dual mortar approach for 3d finite deformation contact with consistent linearization. Int J Numer Meth Eng 83(11):1428–1465
63. Temizer I, Wriggers P, Hughes T (2012) Three-dimensional mortar-based frictional contact treatment in isogeometric analysis with nurbs. Comput Methods Appl Mech Eng 209:115–128
64. Laursen T, Simo J (1993) A continuum-based finite element formulation for the implicit solution of multibody, large deformation-frictional contact problems. Int J Numer Methods Eng 36(20):3451–3485
65. Wriggers P (2006) Computational contact mechanics, 2nd edn. Springer, Berlin
66. Sauer RA, De Lorenzis L (2015) An unbiased computational contact formulation for 3d friction. Int J Numer Methods Eng 101(4):251–280
67. Neto AG, Wriggers P (2020) Numerical method for solution of pointwise contact between surfaces. Comput Methods Appl Mech Eng 365:112971
68. Chavan KS, Lamichhane BP, Wohlmuth BI (2007) Locking-free finite element methods for linear and nonlinear elasticity in 2d and 3d. Comput Methods Appl Mech Eng 196(41–44):4075–4086
69. Propp A, Gizzi A, Levrero-Florencio F, Ruiz-Baier R (2020) An orthotropic electro-viscoelastic model for the heart with stress-assisted diffusion. Biomech Model Mechanobiol 19:633–659
70. Wiesner W, Mortele K (2011) Small bowel ischemia caused by strangulation in complicated small bowel obstruction. ct findings in 20 cases with histo-pathological correlation. J Belg Soc Radiol 94(6):309–314
71. Slater N, Montgomery A, Berrevoet F, Carbonell A, Chang A, Franklin M, Kercher K, Lammers B, Parra-Davilla E, Roll S et al (2014) Criteria for definition of a complex abdominal wall hernia. Hernia 18:7–17

72. Şimşek A, Kocaaslan H, Dirican A, Ateş M (2020) Factors affecting strangulation and necrosis in incarcerated abdominal wall hernias. Cyprus J Med Sci 5(4):279–283
73. Center MSKC (2023) About your abdominal incisional hernia surgery. Accessed 06 Dec 2024. https://www.mskcc.org/cancer-care/patient-education/about-your-abdominal-incisional-hernia-surgery
74. Sghaier A, El Ghali MA, Fradi K, Chahed M, Hamila F, Youssef S (2023) Extensive small bowel necrosis due to congenital para duodenal hernia: A diagnostic and therapeutic challenge: Case report. Int J Surg Case Rep 108:108423
75. Misiakos E, Bagias G, Zavras N, Tzanetis P, Patapis P, Machairas A (2014) Strangulated inguinal hernia. Inguinal Hernia 4:87
76. Keeley J, Kaji A, Kim D, Putnam B, Neville A (2019) Predictors of ischemic bowel in patients with incarcerated hernias. Hernia 23:277–280
77. Attard J-AP, MacLean AR (2007) Adhesive small bowel obstruction: epidemiology, biology and prevention. Can J Surg 50(4):291
78. Strik C, Stommel MW, Schipper LJ, Goor H, Ten Broek RP (2016) Long-term impact of adhesions on bowel obstruction. Surgery 159(5):1351–1359
79. Barth BB, Henriquez CS, Grill WM, Shen X (2017) Electrical stimulation of gut motility guided by an in silico model. J Neural Eng 14(6):066010
80. Barth BB, Shen X (2018) Computational motility models of neurogastroenterology and neuromodulation. Brain Res 1693:174–179
81. Lourenço WJ, Reis RF, Ruiz-Baier R, Rocha BM, Dos Santos RW, Lobosco M (2022) A poroelastic approach for modelling myocardial oedema in acute myocarditis. Front Physiol 13:888515
82. Barnafi NA, Gómez-Vargas B, Lourenço WDJ, Reis RF, Rocha BM, Lobosco M, Ruiz-Baier R, Santos RW (2022) Finite element methods for large-strain poroelasticity/chemotaxis models simulating the formation of myocardial oedema. J Sci Comput 92(3):92

Terms and Conditions

Springer Nature journal content, brought to you courtesy of Springer Nature Customer Service Center GmbH (“Springer Nature”).
Springer Nature supports a reasonable amount of sharing of research papers by authors, subscribers and authorised users (“Users”), for small-scale personal, non-commercial use provided that all copyright, trade and service marks and other proprietary notices are maintained. By accessing, sharing, receiving or otherwise using the Springer Nature journal content you agree to these terms of use (“Terms”). For these purposes, Springer Nature considers academic use (by researchers and students) to be non-commercial.
These Terms are supplementary and will apply in addition to any applicable website terms and conditions, a relevant site licence or a personal subscription. These Terms will prevail over any conflict or ambiguity with regards to the relevant terms, a site licence or a personal subscription (to the extent of the conflict or ambiguity only). For Creative Commons-licensed articles, the terms of the Creative Commons license used will apply.
We collect and use personal data to provide access to the Springer Nature journal content. We may also use these personal data internally within ResearchGate and Springer Nature and as agreed share it, in an anonymised way, for purposes of tracking, analysis and reporting. We will not otherwise disclose your personal data outside the ResearchGate or the Springer Nature group of companies unless we have your permission as detailed in the Privacy Policy.
While Users may use the Springer Nature journal content for small scale, personal non-commercial use, it is important to note that Users may not:

1. use such content for the purpose of providing other users with access on a regular or large scale basis or as a means to circumvent access control;
2. use such content where to do so would be considered a criminal or statutory offence in any jurisdiction, or gives rise to civil liability, or is otherwise unlawful;
3. falsely or misleadingly imply or suggest endorsement, approval , sponsorship, or association unless explicitly agreed to by Springer Nature in writing;
4. use bots or other automated methods to access the content or redirect messages
5. override any security feature or exclusionary protocol; or
6. share the content in order to create substitute for Springer Nature products or services or a systematic database of Springer Nature journal content.

In line with the restriction against commercial use, Springer Nature does not permit the creation of a product or service that creates revenue, royalties, rent or income from our content or its inclusion as part of a paid for service or for other commercial gain. Springer Nature journal content cannot be used for inter-library loans and librarians may not upload Springer Nature journal content on a large scale into their, or any other, institutional repository.
These terms of use are reviewed regularly and may be amended at any time. Springer Nature is not obligated to publish any information or content on this website and may remove it or features or functionality at our sole discretion, at any time with or without notice. Springer Nature may revoke this licence to you at any time and remove access to any copies of the Springer Nature journal content which have been saved.
To the fullest extent permitted by law, Springer Nature makes no warranties, representations or guarantees to Users, either express or implied with respect to the Springer nature journal content and all parties disclaim and waive any implied warranties or warranties imposed by law, including merchantability or fitness for any particular purpose.
Please note that these rights do not automatically extend to content, data or other material published by Springer Nature that may be licensed from third parties.
If you would like to use or distribute our Springer Nature journal content to a wider audience or on a regular basis or in any other manner not expressly permitted by these Terms, please contact Springer Nature at

onlineservice@springernature.com